MEASUREMENTS OF SPIN TORQUES GENERATED BY TOPOLOGICAL INSULATORS AND HEAVY METALS

A Dissertation

Presented to the Faculty of the Graduate School

of Cornell University

in Partial Fulfillment of the Requirements for the Degree of

Doctor of Philosophy

by

Alex Ryckman Mellnik

May 2015

MEASUREMENTS OF SPIN TORQUES GENERATED BY TOPOLOGICAL INSULATORS AND HEAVY METALS

Alex Ryckman Mellnik, Ph.D.

Cornell University 2015

This dissertation discusses measurements of spin torques generated by two classes of materials; heavy metals and topological insulators. In the first half, we use spin torque ferromagnetic resonance with and without the addition of DC currents to measure spin torques generated by the topological insulator bismuth selenide, and find that the effective spin torque ratio, a figure of merit for generating spin torques, is at least of order ~ 1, larger than any other material measurement at room temperature to date. In the second half, we discuss a recently-developed method of measuring spin torques optically using the magneto-optic Kerr effect, and the construction of such an experimental setup at Cornell. This new technique may allow easy measurements of spin torques in systems with insulating ferromagnetic layers, which is not possible with spin torque ferromagnetic resonance. We compare it to spin torque ferromagnetic resonance and other electrical measurements using measurements of platinum / permalloy and bismuth selenide / permalloy bilayers, and find that it is agrees well with other methods.

BIOGRAPHICAL SKETCH

Alex Ryckman Mellnik was born on August 6th, 1986 to parents Ted Alan Mellnik and Patricia Louise Ryckman in Charlotte, North Carolina. A middle child, he grew up between an older sister Kate and a younger brother John in a quiet neighborhood in the University District of Charlotte, and spent much of his early life either reading obsessively or exploring the adjacent woods. His summers were full of adventures, as his family took long trips crisscrossing the country in the family van, traveling as far as Alaska while visiting parks, national forests and camping each night.

Early in his school years, he was an undistinguished student, often bored or restless in class, and was particularly indignant that each year's math class covered largely the same material as the previous year's. In 5th grade his teacher took pity on him and unilaterally transferred him to the advanced math class. After a choppy start, he quickly fell in love with the newly-challenging subject. Around the same time he joined a local Odyssey of the Mind group, and discovered a love for creative problem solving and working as a team.

His family includes an ever-growing number of dedicated and talented librarians, and while he considered joining the merry band, he was also interested in science from an early age. His grandfather, William D. Ryckman, was a retired electrical engineer and lived just down the street. W. D. Ryckman encouraged his young grandson by letting him tag along as he worked in his well-equipped workshop, and even helped him put together simple projects. One of these projects, a variable-frequency resonator hooked up to a neon bulb, taught Alex important lessons about resonance and power dissipation in diodes when it exploded on the kitchen table while he

was showing it to his mom. Before long, he was conducting his own experiments (consisting largely of disassembling electronic devices purchased at yard sales and almost reassembling them) and also began writing his first computer code in QBASIC (which was full of GOTO statements and other computer-science no-nos).

He attended the International Baccalaureate program at Harding University High School, and fell in with other overworked students who showed a level of enthusiasm for activities like Model United Nations seen only for sports teams at other schools. After graduating, he took part in the Congress-Bundestag Youth Exchange program and went to Germany, where he spent a year living in the small village of Mengershausen with a host family, the Müllers, while learning German and studying at a high school and the university in nearby Göttingen.

Upon returning to the United States, he attended the University of North Carolina and immediately dove into a physics major. Near the end of his first semester two important things happened – he started his first real work as a scientist by joining Professor Frank Tsui's Advanced Epitaxial Materials research group, and he was introduced to another freshman recently returned from Europe, Caitlin Cox. Four years later Alex and Caitlin decamped to Ithaca, New York to pursue graduate studies, where Alex joined Professor Dan Ralph's research group. Caitlin and Alex were married in the summer of 2014, and are currently looking forward to their next adventure together.

To my family and my wife, for their continued love and support.

ACKNOWLEDGMENTS

This dissertation is possible because of the continuous support and encouragement I received at every step of my studies, as well as the combined efforts of many other researchers at Cornell and other institutions.

As a junior in high school, I visited the University of North Carolina with my father. I was still undecided as to what I would like to study, but since I enjoyed my high school physics courses, we dropped by the physics department on a whim. Even though we didn't have an appointment, one professor graciously took more than an hour to meet with us and answer all my questions about UNC, the department, and studying physics in general.

Three years later, as a freshman physics major at UNC, I told the instructor of my electricity and magnetism class, Professor John Hernandez, that I was interested in research and asked how I might join a group. He told me that I should ask around on my own, but apparently recommended me at a faculty meeting and asked if anyone had a position for an undergraduate researcher. One professor responded that he could take on a student, and I joined the Tsui lab.† The Tsui group immediately accepted me as another member of the team, and by the end of my second year I was independently fabricating microelectronic devices at Duke University's Shared Materials Instrumentation Facility.

My senior year at UNC, I flew up to Ithaca to visit Cornell University. Even though it wasn't an official visiting time (it may have even been the day before Thanksgiving), one professor took an hour out of his busy schedule to talk with me about his work and the program, show me around

† I actually worked in the Tsui lab for several months before I realized he was the same professor who had shown me around three years before.

the tab and shared facilities, and introduced me to his graduate students. At the end of the visit, he even encouraged me to contact his students and even ask them if he was a good advisor to work for. I didn't bother – by then I knew that he was exactly the sort of scientist I hoped to work with. Ten days after graduating from UNC, I moved to Ithaca and started working for Professor Dan Ralph. Nearly six years later, I can say for certain that it was a good choice.

In the Ralph group I have had the honor of working with many talented researchers, and are thankful for their incredible assistance and support. Yongtao Cui helped me get started with fabrication at the Cornell Nanoscale Science and Technology Facility (CNF), and Yongtao, Lin Xue and Chen Wang all were instrumental in helping me make my first measurements. Sufei Shi taught me to always look for interesting questions and new areas to research, and continues to be an excellent resource. While I did not work as closely with Takahiro Moriyama, Eugenia Tam, Wan Li, Josh Parks and Kiran Thadini, they were all excellent lab mates and helped make the group a great one to work in. I joined the lab around the same time as Ted Gudmundsen, who's willingness to talk through any interesting problem, related to physics or not, made his office a go-to location whenever I had something I wanted to mull over. Colin Heikes also joined the lab around the same time, and has been my go-to resource for any question related to materials science (or craft beer). I have also had the opportunity to work with many students and post-docs who joined the lab after me, including Greg Stiehl, David MacNeill, Colin Jermain, John Heron, Sriharsha Aradhya, and Marcos Guimaraes.

When I started at Cornell, the Ralph group was low on desk spaces, and Dan suggested that I set up a desk in the vacant microkelvin area of the basement, and then move in to a normal office when someone graduated in a few months. I moved in to microkelvin, and quickly came to love

the industrial décor, convenient tools and work areas, and the fact that it has the only two windows in the basement. Microkelvin has also become the home for the graduate students with whom I've worked most closely on my research projects – Jennifer Grab, Jonathan Gibbons and Neal Reynolds,† as well as two exceptionally talented undergraduate researchers, Peter Mintun (now at the University of Chicago) and Alison Rugar. Microkelvin has been my home away from home for the past several years, and it's been a great place to work as well at the location of many wonderful side projects (such as building a giant unicorn to invade Dragon Day with).

I have had many fruitful collaborations outside of the Ralph group, and nearly everyone in our group has worked closely with the students in Professor Robert Buhrman's research group. Professor Buhrman, Junbo Park, Praveen Gowtham, Graham Rowlands, Luqiao Liu, Minh-Hai Nguyen, Luis Henrique Vilela Leão, Yongxi Ou and Chi-Feng Pai have been valuable resources and a joy to work with. Professor Eun-Ah Kim and her research group, especially Mark Fischer, were our theoretical collaborators, and they were able to build a model for the interaction between topological insulators and magnets which helped us understand our system. Matt Bierbaum and Alex Alemi, students in Professor Jim Sethna's group, were instrumental in figuring out how to run micromagnetic simulations and the best way to perform challenging fits.

Cornell is an excellent place to do research, and much of this is due to their great facilities and technical staff. The Cornell Center for Materials Research (CCMR) makes it possible for us to perform new and challenging measurements by just checking out what we need from their lending library, rather than needing to spend hundreds of thousands of dollars on new equipment. People like Jon Shu, Steve Kriske and Mick Thomas keep everything running smoothly and are

† Neal's office is actually not in microkelvin, but we'll count him as an honorary member.

great resources. Similarly, CNF is one of the best research cleanrooms in the world, and their talented staff make it possible. Rob Illic, Alan Bleier, Daron Westly, Garry Bordonaro, Beth Rhoades, Noah Clay and Jerry Drumheller have been particularly helpful keeping equipment running and figuring out processes.

Outside of Cornell, I've had the opportunity to work closely with Professor Nitin Samarth and his group at Penn State, especially Anthony Richardella and Abhinav Kandala. These talented materials scientists and physicists have kept us in a constant supply of bismuth selenide† and new exciting ideas for research. More recently I started working with Professors John Q. Xiao and Virginia Lorenz's groups at Delaware, particularly their former post-doc, Xin Fan, who is now a professor at the University of Denver. Xin Fan has an incredible skill for developing new measurement techniques, and I have been fortunate to work with him on our MOKE collaboration.

Ithaca has been a wonderful place to attend graduate school, and despite minor gripes about the weather, it's been a blast. I have become friends with many exceptional people – other students in a range of departments and people in the greater community though activities like jiu jitsu. Many thanks to everyone who's helped make my graduate studies an exceptional and enjoyable experience.

† My graduate research really only took off after I stopped growing my own bismuth selenide nanostructures and switched to their MBE-grown thin films.

Table of contents

1. Magnetic Memory and Spin Torques

This chapter give a brief introduction to spin torques and discusses how they relate to a very practical goal – to develop better solid state magnetic memories. Spin torques can be generated using spin-polarized charge currents, although for many situations it is more desirable to generate them using pure spin currents. We discuss three different possible ways to generate pure spin currents, including using the surface states of topological insulators.

1.1 The dream of universal memory

Modern computers contain a hierarchy of memory types adapted to the wide range of time- and size-scales required for retrieving and storing different information.[1] For example, consider the computer that I am using to draft this document. The fastest memory is the collection of CPU registers that store information as they are operated on, with a timescale of ~0.3 ns. Next, the processor contains three tiers of cache made from static random-access memory which range from the fastest: level one cache which has 64 KB for each core, to the slowest: level three cache with 6 MB shared between the four cores.[2] Slower still is the primary active memory, 8 GB of dynamic random-access memory (DRAM) with a latency of ~10 ns. These first types of memory are volatile, and require constant refreshing and power to maintain their information. There's also nonvolatile memory, including a solid state drive which can store 120 GB but with a latency of ~100 ns,[3] and a hard disk drive with seek times of ~10 ms, roughly 30,000 times slower than the fastest memory in the computer.

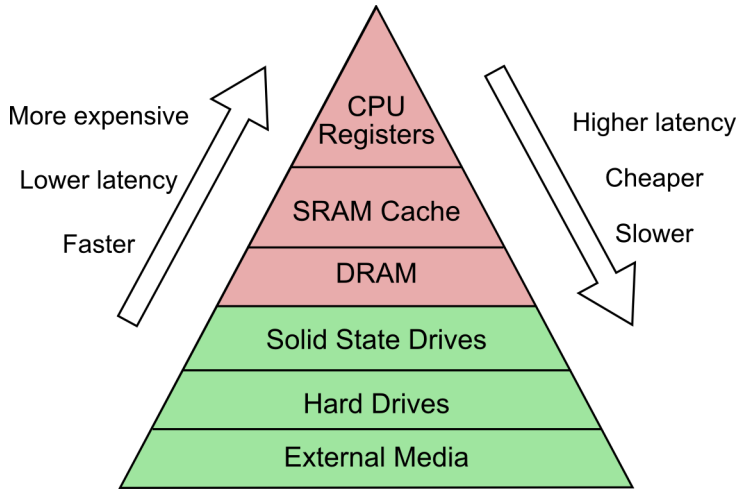

Figure 1.1. The "pyramid" of memory types found in modern computers. After reference 1. Most information is stored in the slower nonvolatile memory types marked in green, while nonvolatile memories are marked in red. The pyramid is not to scale, and each descending level represents a roughly 10× increase in storage capacity in a typical system.

This pyramid of memories, from small, fast, volatile and expensive to large, slow, nonvolatile and cheap, is a product of necessity. To date, there is no single type of memory that satisfies every requirement simultaneously, but that hasn't stopped scientists and engineers from dreaming of a *universal memory* which could combine the high storage density and nonvolatility of solid state drives and hard drives with the fast access times of synchronous dynamic random access memory (SDRAM). The closest widely-commercialized analog to a universal memory today is the NAND flash that powers solid state drives, but these will never be a suitable replacement for SDRAM as each bit can only be written ~1000 times in current-generation devices (although careful distribution of write loads allows them to last at least as long as hard drives under similar use levels).[4]

There are, however, many alternative memory technologies in various stages of development that have been touted as potential universal memories. A few of the most notable are

- Phase change memory, which relies on alloys like germanium-tin-telluride which can reversibly switch between amorphous and crystalline states with high and low resistivity respectively.[5,6]

- Resistive random-access memory, which uses the fact that electrical currents can be used to move ions in metal oxides and chance their low-bias resistance.[7]

- Racetrack memory, which writes bits as domains in a magnetic nanowire and reads them by driving the domain walls past a stationary sensor using an electric current.[8,9]

1.2 Magnetoresistive random-access memory (MRAM)

One particularly promising† candidate for a universal memory is the class of technologies known as magnetoresistance random-access memory (MRAM). MRAM is the solid state analog of a hard disk drive – it stores information in the magnetization state of a nanometer-scale magnet, and reads and writes the state electronically, without any moving parts.

Reading the state of a MRAM bit is now relatively simple thanks advances in the tunneling magneto-resistance effect (TMR). In almost all current readout designs, the active layer of a memory cell is built into a tunnel junction with a second pinned magnetic layer as the opposing electrode. With carefully-chosen magnetic materials and a spin-filtering tunnel barrier such as MgO, the resistance can change by more than 5× between the two magnetic states at room temperature.[10]

Changing the state of a MRAM is significantly more challenging, and the focus of much ongoing research. Early MRAM designs switched bits using magnetic fields, analogous to how write

† I might be somewhat biased in this regard.

heads in hard drives switch regions of the recording media. In this design, an array of in-plane current "word" lines is positioned above each bit, and a second array of word lines is positioned below each bit perpendicular to the first array. Flowing current through any single line does not produce a sufficient field to flip any bit, but flowing current through two perpendicular lines creates a large enough field to flip the bit at their intersection.[11] A schematic diagram of a typical bit is shown in Figure 1.2.

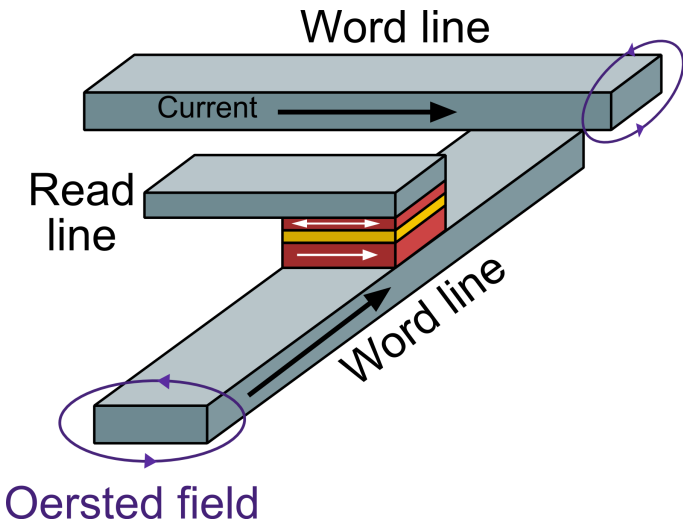

Figure 1.2. A typical bit in field-driven MRAM, after a diagram in Chappert et al.[12] *Two magnetic layers (red) are separated by a tunnel junction (yellow). The moment of the bottom magnetic layer is pinned but the upper layer is free to switch. When current flows through both perpendicular word lines, the combined Oersted field is sufficient to switch the free magnetic layer back and forth. The orientation of the free layer is read out via the TMR by flowing a much smaller current between the lower word line and the read line.*

This design is straightforward to implement, but comes with a host of problems. It is difficult to avoid accidentally switching other bits positioned along active word lines since they see nearly the same field as the bit meant to be switched. It is also difficult to scale the word lines down to smaller sizes or larger arrays without also greatly increasing the power required to flip each bit.[13,14] While several companies demonstrated MRAM prototypes and sold specialized MRAM

devices using this technology,[11] it never entered widespread use.

1.3 Spin transfer torque and MRAM

A second way forward appeared in 1989. John C. Slonczewski, then a researcher at IBM's Watson Research Center, published a theoretical study of two magnetic materials separated by an insulating barrier. In addition to several previously-observed effects, he predicted that for a non-zero external bias, angular momentum would flow from one magnetic layer to the other, and could even generate "a pumping action which can cause spontaneous growth of magnetic oscillations."[15] At the time magnetic tunnel junctions were still in their infancy, but the effect gained widespread attention[16] when it was later extended to systems with a metallic spacer rather than a tunnel junction between the two magnetic layers, and was predicted to be strong enough to flip the magnetization of one layer.[17,18] After progressive advances from several research groups, switching of nanometer-scale patterned magnets with metallic spacers was demonstrated in 2000,[19] and by 2004 switching was also demonstrated in tunnel junctions.[20,21]

The effect that is the basis for these devices is known as *spin transfer torque*. When current flows through a magnetic layer it can pick up a spin polarization due to the difference in scattering rates for spins aligned or misaligned with the moment. When such a spin-polarized current enters a second magnetic layer with a different alignment, the spins which are misaligned with the moment will preferentially scatter, transferring angular momentum and applying a magnetic torque to the moment of the second (free) layer. Magnetic torques (written here as torque per unit moment) are defined as

$$\vec{\tau} = \frac{1}{M_s} \frac{d\vec{M}_{free}}{dt} \tag{1.1}$$

The maximum torque this process can apply is proportional to both the spin polarization of the incoming current, P, and the magnitude of that current, I_C

$$\tau_{max} = P I_C \frac{\hbar}{2e} \frac{\gamma}{M_s Vol_{mag}} \tag{1.2}$$

where Vol_{mag} is the volume of the free layer.

In two-terminal devices where the write and the read paths are the same, the materials properties and other parameters must optimized to maximize both the torques for writing and the TMR for reading the signal out.† Much progress has been made on this front, and in 2012 Everspin released the first commercial spin torque-driven MRAM module,[22] and while it is currently limited to niche applications‡ due to its high cost, low density, and high power consumptions, work is continuing.[23]

1.4 Separating charge and spin transport

Spin torque MRAM continues to improve, but any device powered by a spin-polarized current will always be constrained by Formula 1.2 – for every $\hbar/2$ of angular momentum delivered to the device, at least e charge must flow through the device.ℵ This charge current leads to heating

† A three-terminal device allows these two requirements to be optimized independently, but comes with several drawbacks like larger cell sizes and complexities.

‡ ST-MRAM's high speed and nonvolatility makes it useful in mission-critical applications, and its radiation hardness is perfect for satellites.

ℵ In theory, it is possible to exceed this limit slightly in some special cases.

and resistive losses. The angular momentum required to flip the free layer in a device can be reduced in many ways, but can only be lowered to some finite level without compromising the stability of the bit.

This is not a universal limitation, but is only due to the fact that this type of MRAM relies on *spin polarized charge currents*. This restriction can be lifted by if instead we use *pure spin currents*, in which there is net flow of spin but no net flow of charge, to flip the free layer in our devices. The difference between spin polarized charge currents and pure spin currents is illustrated in Figure 1.3

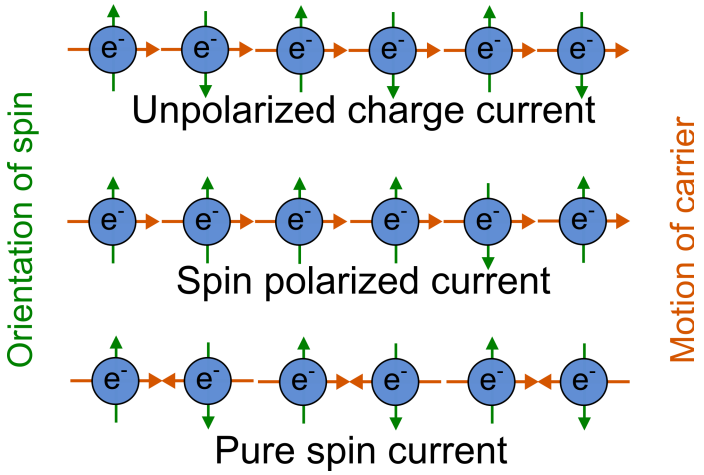

Figure 1.3. Differences between different types of currents. The first row shows an unpolarized charge current, where spins are randomly and evenly distributed between the two orientations, and all carriers move in the same direction due to an electric field. The second row shows a spin polarized current, where all carriers still move in the same direction, but the spins are now mostly in a single orientation. The last row shows a pure spin current, where spins of one orientation move in one direction, and spins of the opposite orientation move in the other direction. There is no net flow of charge but there is a net flow of angular momentum.

Pure spin currents are less straightforward to generate than spin polarized charge currents, but there are several possible ways to generate them that we discuss here.

1.5 The Spin Hall Effect

When a charge current flows through a material with spin-orbit coupling, carriers will scatter preferentially in a direction determined by the orientation of their spin. This phenomena was predicted in 1971,[24] and is now known as the s*pin Hall effect*.[25] For a charge current flowing in wire, these spins scatter until they reach the outside of the wire, where a spin accumulation develops as the influx of spins is balanced by their relaxation. This is analogous to the normal Hall effect where charges with opposite sign accumulate on either side of a channel in the presence of a perpendicular magnetic field. The orientation of the spins on the surface is perpendicular to both the surface normal and the direction of the current flow, as shown schematically in Figure 1.4.

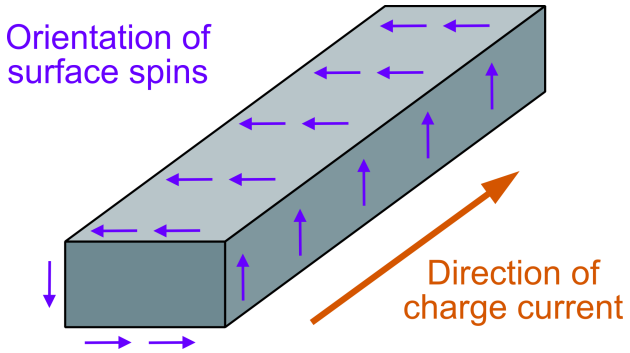

Figure 1.4. Schematic diagram of the spin Hall effect. As a charge current flows in the wire, carriers are preferentially scattered in different directions determined by their spin, which leads to a spin accumulation on the surface with the orientation of the spins perpendicular both to the surface normal and the direction of charge current flow.

This effect was first observed in a very dramatic way – in 2004 the Awschalom group at UCSB used the magnetooptic Kerr effect (see Chapter 4) to directly image the spins that built up on either side of a gallium arsenide channel when a charge current flowed through it.[26] Two years later, Valenzuela & Tinkham performed the first electrical measurements[27] of the spin Hall effect using its analog – the inverse spin Hall effect. They used a ferromagnetic contact to inject a

spin-polarized current into a thin aluminum wire, and used a non-local voltage measurement with a second magnetic contact to study the resulting spin current. While these initial measurements confirmed the existence of the spin Hall effect, quantitative measurements of its strength in different materials were not possible until several years later (with several missteps along the way).[28] The primary figure of merit for generating spin currents using the spin Hall effect is the spin Hall ratio (also known as the spin Hall angle) defined as $\theta = J_S / J_C$, the ratio of the forward-traveling charge current density to the perpendicularly-traveling spin current density. In actual device it is often easier to discuss the effective spin Hall ratio, which uses the portion of the spin current not reflected at the interface between the active material and a magnetic sensor. This value is ~0.07 in platinum for common metallic magnetic sensor layers.[28]

The spin Hall effect is an ideal system for generating and accessing pure spin currents, and was soon put to use applying torques to magnetic layers. In 2011 the Cornell collaboration reported driving ferromagnetic resonance in a permalloy layer using the spin Hall effect in platinum,[29] and shortly thereafter a European collaboration demonstrated switching in a thin cobalt/platinum bilayer[30] which was later attributed to the spin Hall effect.[31]

While platinum has been the canonical heavy metal for studying the spin Hall effect, even larger effective spin Hall effects have been observed in other heavy metals, including spin Hall ratios of ~0.15 in β-tantalum[32] and ~0.3 in β-tungsten.[33] In these studies, the spin torque was also used to switch nanometer-scale magnetic pillars, the basis for a spin Hall effect-driven MRAM bit.

1.6 The Rashba Effect

In a two-dimensional electronic system (2DES) with significant in-plane symmetry and broken

out-of-plane symmetry, spin orbit coupling breaks the degeneracy between states with different spin, resulting in what is now known as the Rashba effect.[34] With the addition of the Rashba term, the Hamiltonian for such a system is[35]

$$H = \frac{p^2}{2m_e} - \frac{\lambda}{\hbar}\vec{\sigma}\cdot\left(\hat{z}\times\vec{p}\right) \qquad 1.3$$

where λ is a constant that describes the strength of the Rashba coupling, m_e is the effective mass, and $\hat{z}$ is the normal unit vector. The schematic band structure is shown in Figure 1.5.

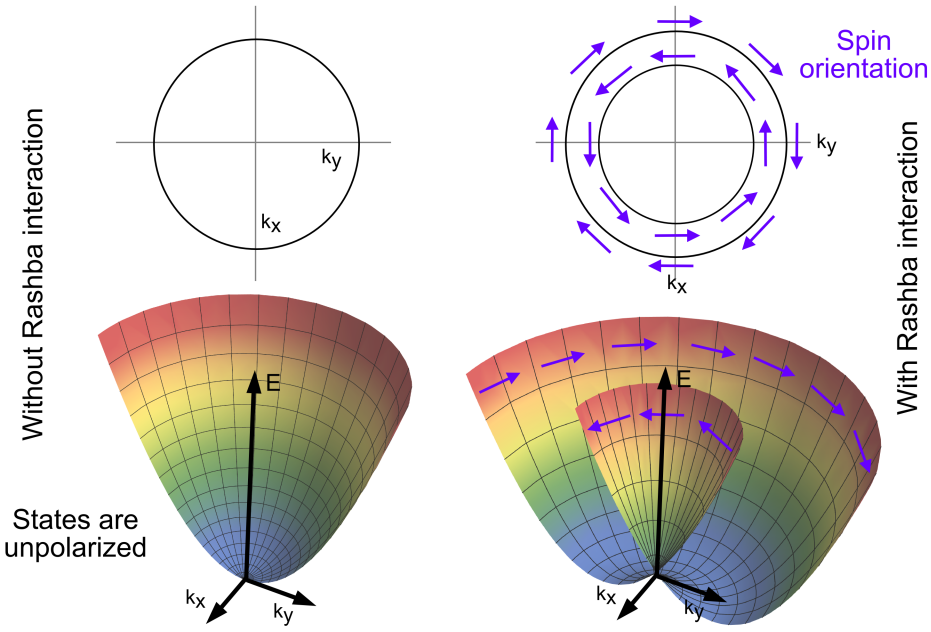

Figure 1.5. Schematic diagram of Rashba split surface states, after Krupin et al.[36] *The upper panels show a "top-down" diagram of the surface states at the Fermi level, while the lower two show a cross-section of the band structure for the two in-plane directions. The Rashba interaction breaks spin degeneracy in the Hamiltonian .*

Spin and momentum are coupled, and an electric current flowing in the plane will generate a spin polarization oriented perpendicular to the direction of the current. (The inverse is also true, and a spin accumulation can be used to generate a current).[37,38] This effect can also occur in magnetic

materials, where spin-orbit coupling adds a perturbation to the normally-uniform spin texture due to the exchange interaction.[39]

Spin accumulations generated via the Rashba effect can apply spin torques to adjacent magnetic layers (or the layer itself if magnetic).[39] To first order, these generate a "field-like", out-of-plane torque.[40] These torques can occur in systems where the spin Hall effect also plays a role, which can lead to miss-identification of the primary source of the torques.[30,31]

1.7 Topological insulator surface states

A topological insulator is a material which has a bulk band gap and special surface states which traverse the bulk gap. In the interior of the material, the band structure appears identical to that of a normal insulator, except that some states above and below the gap are *inverted* – reversed from what their positions would be in the absence of spin orbit coupling (or another perturbation[41]). At the surface of the material these bands revert to their unperturbed positions, and cross the bulk gap, creating states that exist only at the boundary of the material.[42] Carriers in these states have their spins locked perpendicular to their momentum, and their existence is protected against perturbations.[43] The band structure of a topological insulator is shown schematically in Figure 1.6.

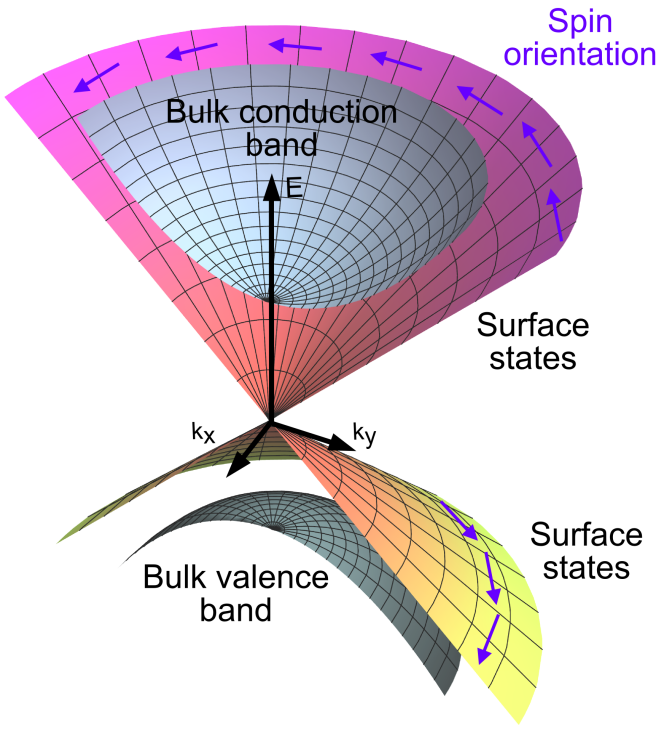

Figure 1.6. Schematic diagram of the band structure of a topological insulator. A Dirac cone of surface states traverses the bulk band gap. Carriers in the surface states have their spin locked perpendicular to their momentum, and the winding of spins has opposite handedness above and below the Dirac point.

The spin structure of a topological insulator surface state away from the Dirac point is similar one of the rings of states in a Rashba-split 2DES. Similarly, charge currents are coupled to spin accumulations (and the inverse),[44] and flowing charge currents through the surface states of a topological insulator are expected to apply torques to adjacent magnetic layers.[44–47]

The spin Hall effect and Rashba effects are expected to occur simultaneously in some systems, and similarly Rashba-split 2DES are often observed to coexist with topological surface states in topological insulators.[48–50]

2. Ferromagnetic Resonance Theory and Calculations

In the first chapter, we learned that spin torques can change and even flip orientation of a magnetic material. In order to measure and characterize spin torques, we first need to know exactly how the response of a magnet relates to the spin torques that act on it, and further how this response relates to some easily-measurable signal, such as a voltage. To do this, we perform a number of calculations all based on the Landau-Lifchitz-Gilbert-Slonczewski equation which describes the dynamics of a magnetic moment under spin torques and external magnetic fields.

We derive the magnetic response of a thin in-plane magnetized film when RF and DC torques are applied. Mirroring our experiments in later chapters, we use a bilayer geometry where current flows through both a the ferromagnetic layer and an adjacent active layer, and an external magnetic field is applied in-plane.

2.1 Coordinate system and conventions

The coordinate system we use in this chapter is shown in Figure 2.1. The unprimed coordinates are based on the orientation of the DC component of the moment (mostly aligned with the external field), so that the average moment points in the y direction. The primed coordinates match the geometry so that the current flow is in the y' direction.

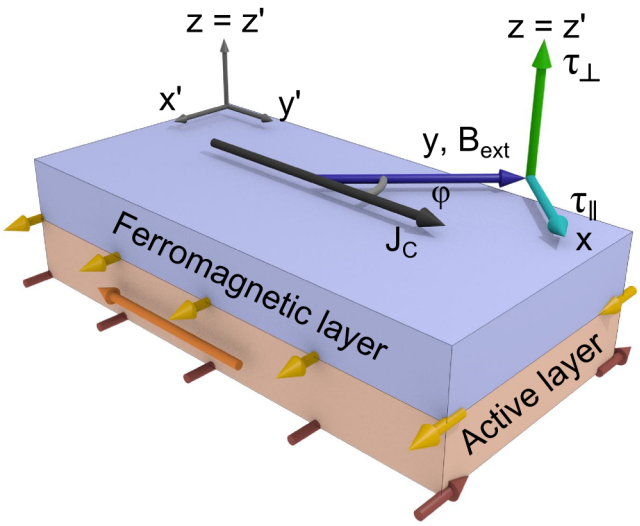

Figure 2.1. Illustration of the coordinate system used in this chapter. Current flows through the bilayer in the y' *direction and the external magnetic field,* B_{eff} *, is applied in the* y *direction.*

All equations in this chapter are expressed in MKS units.

2.2 Spin torque ferromagnetic resonance (ST-FMR)

At the right combination of external magnetic field and driving torques, the moment of a magnetic material will oscillate. This was first observed as a change in microwave absorption at radio frequencies.[51] In the case of a thin film with the moment in-plane, the resonance frequency is given by $\omega_0^2 = \gamma^2 B_{ext}(B_{ext} + \mu_0 M_{eff})$ where ω_0 is the resonant field, γ is the gyromagnetic ratio, and M_{eff} is the effective saturation magnetization. Beginning in the mid 2000's, ST-FMR was used to quantify spin torques in spin valves and magnetic tunnel junctions.[52–54]

We model ferromagnetic resonance for a magnetic domain by using the Landau-Lifchitz-Gilbert-Slonczewski (LLGS) equation.[17] For an applied field and a unit moment almost entirely in the *y* direction, $\hat{m}(t) = \vec{M}(t)/M_s = m_x(t)\hat{x} + \hat{y} + m_z(t)\hat{z}$, with *z* normal to the film plane and arbitrary torques per unit moment in the *x* and *z* directions

$$\dot{\hat{m}} = -\gamma \hat{m} \times \vec{B}_{eff} + \alpha \hat{m} \times \dot{\hat{m}} + (\tau_{\parallel, RF} + \tau_{\parallel, DC}) \frac{\hat{m} \times (\hat{x}' \times \hat{m})}{|\hat{x}' \times \hat{m}|} + (\tau_{\perp, RF} + \tau_{\perp, DC}) \frac{\hat{x}' \times \hat{m}}{|\hat{x}' \times \hat{m}|}$$
$$= -\gamma \hat{m} \times \left(\vec{B}_{ext} - \mu_0 \hat{m} \cdot \hat{z} M_{eff} \hat{z}\right) + \alpha \hat{m} \times \dot{\hat{m}} + (\tau_{\parallel, RF} + \tau_{\parallel, DC}) \frac{\hat{m} \times (\hat{x}' \times \hat{m})}{|\hat{x}' \times \hat{m}|} + (\tau_{\perp, RF} + \tau_{\perp, DC}) \frac{\hat{x}' \times \hat{m}}{|\hat{x}' \times \hat{m}|} \quad 2.1$$

Here, for the case of spin-transfer torque, we have rewritten the torque in the *x* direction in terms of *x′*, the orientation of the applied spins. Note that

$$|\hat{x}' \times \hat{m}| = \sqrt{m_{z0}^2 \sin^2(\varphi) + m_{z0}^2 \cos^2(\varphi) + \cos^2(\varphi) + m_{x0} \sin(\varphi) \cos(\varphi) + m_{x0}^2 \sin^2(\varphi)} \approx |\cos(\varphi)| \quad 2.2$$

which is an approximation we need to make to get a solution in a closed form. If we assume moments and torques of the form $m_x = m_{x0} e^{i\omega t}$ and ignore higher-frequency components, we get two equations for the components of the moment (the one for the *y* component is trivial)

$$0 = (B_{ext} + \mu_0 M_{eff}) m_{z0} \gamma - \tau_{\parallel, RF} - \tau_{\parallel, DC} - i m_{x0} \omega + i m_{z0} \alpha \omega + (m_{x0} \tau_{\parallel, DC} - m_{z0} \tau_{\perp, DC}) \tan(\varphi)$$
$$0 = -B_{ext} m_{x0} \gamma - \tau_{\perp, RF} - \tau_{\perp, DC} - i m_{z0} \omega - i m_{x0} \alpha \omega + (m_{x0} \tau_{\perp, DC} + m_{z0} \tau_{\parallel, DC}) \tan(\varphi) \quad 2.3$$

The first thing to notice is that the DC out-of-plane torque looks just like a modification of the applied field. To save space we define $B' = B_{eff} - \tau_{\perp, DC} \tan(\varphi)/\gamma$ which reduces our two formulas to

$$\gamma (B' + \mu_0 M_{eff}) m_{z0} + m_{x0} \tau_{\parallel, DC} \tan(\varphi) - i m_{x0} + i \alpha m_{z0} \omega = \tau_{\parallel, RF}$$
$$\gamma B' m_{x0} + i \omega (\alpha m_{x0} + m_{z0}) + \tau_{\perp, RF} = m_{z0} \tau_{\parallel, DC} \tan(\varphi) \quad 2.4$$

Solving for the moments gives in its full form

$$m_{x0} =$$

$$\frac{-i\alpha\tau_{\perp,RF}\omega - \gamma(B' + \mu_0 M_{eff})\tau_{\perp,RF} + \tau_{\parallel,RF}\tau_{\parallel,DC}\tan(\varphi) - i\tau_{\parallel,RF}\omega}{\gamma^2 B'(B' + \mu_0 M_{eff}) + 2i\alpha\gamma\omega B' - \omega^2(1+\alpha^2) + i\alpha\gamma\omega\mu_0 M + \tau_{\parallel,DC}^2\tan^2(\varphi) - 2i\omega\tau_{\parallel,DC}\tan(\varphi)}$$

$$m_{z0} =$$

$$\frac{i\omega(\alpha\tau_{\parallel,RF} - \tau_{\perp,RF}) + \gamma B'\tau_{\parallel,RF} + \tau_{\parallel,DC}\tau_{\perp,RF}\tan(\varphi)}{\gamma^2 B'(B' + \mu_0 M_{eff}) + 2i\alpha\gamma\omega B' - \omega^2(1+\alpha^2) + i\alpha\gamma\omega\mu_0 M_{eff} + \tau_{\parallel,DC}^2\tan^2(\varphi) - 2i\omega\tau_{\parallel,DC}\tan(\varphi)}$$

2.5

Only the real component of the moment has any physical meaning, and in many situations we only care about the portion of the real component which is in-phase with the driving current, although for some things we need to know the full time-dependence of the moment. The full real components of the above are very long, but can be found easily in Mathematica. For the highest-possible accuracy in sensitive measurements such as the DC mixing measurements, it doesn't hurt to use the exact version of these formulas. In most situations it is safe to make several good approximations. First, we can take the above and assume that $\alpha^2 \ll 1$ and also that anything higher-order in the torques can be neglected, which corresponds to the small-angle excitation regime. Then we have

$$m_{x0} = \frac{-i\alpha\tau_{\perp,RF}\omega - \gamma(B' + \mu_0 M_{eff})\tau_{\perp,RF} - i\omega\tau_{\parallel,RF}}{\gamma^2 B'(B' + \mu_0 M_{eff}) + 2i\alpha\gamma\omega B' - \omega^2 + i\alpha\gamma\omega\mu_0 M_{eff} + 2i\omega\tau_{\parallel,DC}\tan(\varphi)}$$

$$m_{z0} = \frac{\gamma B'\tau_{\parallel,RF} + i\omega(\alpha\tau_{\parallel,RF} - \tau_{\perp,RF})}{\gamma^2 B'(B' + \mu_0 M_{eff}) + 2i\alpha\gamma\omega B' - \omega^2 + i\alpha\gamma\omega\mu_0 M_{eff} + 2i\omega\tau_{\parallel,DC}\tan(\varphi)}$$

2.6

We can take the time-dependent real components of these again using the fact that $\alpha^2 \ll 1$ and getting rid of higher-order terms in the torques and get something which almost fits on the page

$$\Re(m_x)=$$

$$\frac{\cos(\omega t)(-\gamma\omega^2\tau_{\perp,RF}(B'+\mu_0 M_{eff})+\gamma^3\tau_{\perp,RF}B'(B'+\mu_0 M_{eff})^2-\alpha\gamma\omega^2(2B'+\mu_0 M_{eff})\tau_{\parallel,RF})}{(\omega^2-\gamma^2 B'(B'+\mu_0 M_{eff}))^2+\omega^2(\gamma^2\alpha^2(2B'+\mu_0 M_{eff})^2-4\alpha\gamma\tau_{\parallel,DC}(2B'+\mu_0 M_{eff})\tan(\varphi))}$$

$$+\frac{\omega\sin(\omega t)(-\omega^2(\alpha\tau_{\perp,RF}+\tau_{\parallel,RF})+\gamma^2(B'+\mu_0 M_{eff})(\gamma B'\tau_{\parallel,RF}-\alpha\gamma\tau_{\perp,RF}(B'+\mu_0 M_{eff})))}{(\omega^2-\gamma^2 B'(B'+\mu_0 M_{eff}))^2+\omega^2(\gamma^2\alpha^2(2B'+\mu_0 M_{eff})^2-4\alpha\gamma\tau_{\parallel,DC}(2B'+\mu_0 M_{eff})\tan(\varphi))} \quad 2.7$$

$$\Re(m_z)=$$

$$\frac{\cos(\omega t)(-\gamma\omega^2 B'\tau_{\parallel,RF}+\gamma^3 B'^2\tau_{\parallel,RF}(B'+\mu_0 M_{eff})-\alpha\gamma\omega^2\tau_{\perp,RF}(2B'+\mu_0 M_{eff}))}{(\omega^2-\gamma^2 B'(B'+\mu_0 M_{eff}))^2+\omega^2(\gamma^2\alpha^2(2B'+\mu_0 M_{eff})^2-4\alpha\gamma\tau_{\parallel,DC}(2B'+\mu_0 M_{eff})\tan(\varphi))}$$

$$+\frac{\omega\sin(\omega t)(\omega^2(\alpha\tau_{\parallel,RF}-\tau_{\perp,RF})+\gamma B'(\alpha B'\tau_{\parallel,RF}+\gamma\tau_{\perp,RF}(B'+\mu_0 M_{eff})))}{(\omega^2-\gamma^2 B'(B'+\mu_0 M_{eff}))^2+\omega^2(\gamma^2\alpha^2(2B'+\mu_0 M_{eff})^2-4\alpha\gamma\tau_{\parallel,DC}(2B'+\mu_0 M_{eff})\tan(\varphi))}$$

In this form we can easily see that the resonant field is given by $\omega_0^2=\gamma^2 B'(B'+\mu_0 M_{eff})$ as expected, and that the damping term, approximately equal to the linewidth squared, is

$$\omega^2(\gamma^2\alpha^2(2B'+\mu_0 M_{eff})^2-4\alpha\gamma\tau_{\parallel,DC}(2B'+\mu_0 M_{eff})\tan(\varphi)) \quad 2.8$$

which includes both the normal damping and also the damping-like contribution from the DC in-plane torque. It is important to note the extra contribution from $\tau_{\perp,DC}$ cannot be treated like a modification to α the way that we can treat the DC out-of-plane torque as a modification of the field, since it is coupled with α and has a different field dependence.

2.3 Moment products for spin pumping

A precessing magnetic moment also generates pure spin currents. As a moment precesses it continuously loses angular momentum to damping, some of which can be transferred to adjacent layers.[55]

For ST-FMR, all we need to know about the moment is is $\Re(m_{x0})$ which we found above. In spin pumping the important quantity is the pumped spin which is given by[56]

$$j_s \hat{s} = \frac{\hbar}{4\pi} \Re\left(g_{\uparrow\downarrow}^{eff}\right) \left(\vec{m}(t) \times \frac{d\,\vec{m}(t)}{d\,t} \right) \tag{2.9}$$

where $\Re(g_{\uparrow\downarrow}^{eff})$ is the effective real component of the spin mixing conductance for the interface. For now we assume that the imaginary component of the spin-mixing conductance is small. The moment crossed with its time derivative has several components. Crossing the *y* component of the unit moment ($\hat{y}$) with $d\,m_x(t)/dt$ or $d\,m_z(t)/dt$ gives an AC pumped spin; this is the basis of the AC spin pumping effect. Crossing one of the time-dependent components with the time-derivative of the other gives a DC spin current in addition to higher-order effects; this is the basis of the DC spin pumping effect.

For DC spin pumping we have

$$\begin{aligned} &\int_0^{2\pi/\omega} \left(\vec{m}(t) \times \frac{d\,\vec{m}(t)}{d\,t} \right) dt = \int_0^{2\pi/\omega} \left(m_z(t) \frac{d\,m_x(t)}{dt} - m_x(t) \frac{d\,m_z(t)}{dt} \right) dt\, \hat{y} \\ &= \frac{\gamma \omega^2 \left(B' \left(\tau_{\parallel,RF}^2 + \tau_{\perp,RF}^2 \right) + \mu_0 M_{eff}\, \tau_{\perp,RF} \left(\tau_{\perp,RF} - \tau_{\parallel,RF} \right) \right)}{\left(\omega^2 - \gamma^2 B' \left(B' + \mu_0 M_{eff} \right) \right)^2 + \omega^2 \left(\gamma^2 \alpha^2 \left(2B' + \mu_0 M_{eff} \right)^2 - 4\alpha\gamma\tau_{\parallel,DC} \left(2B' + \mu_0 M_{eff} \right) \tan(\varphi) \right)} \hat{y} \end{aligned} \tag{2.10}$$

The vector quantity represents the orientation of the spins being pumped, not their direction of travel. DC spin pumping always produces spins that are aligned with the main component of the moment.

For AC spin pumping we have, making the same approximations as before,

$$\left(\vec{m}(t)\times\frac{d\,\vec{m}(t)}{d\,t}\right)_{AC}=\frac{d\,m_z(t)}{dt}\,\hat{x}-\frac{d\,m_x(t)}{dt}\,\hat{z} \tag{2.11}$$

We don't care about the phase of the resulting AC signal, the only thing that matters for measurements is the magnitude of the sinusoidal pumped spin in each direction which is

$$\left|\frac{d\,m_z(t)}{dt}\right|\hat{x}+\left|\frac{d\,m_x(t)}{dt}\right|\hat{z}=$$

$$\omega\sqrt{\frac{\omega^2(\alpha\tau_{\parallel,RF}-\tau_{\perp,RF})^2+\gamma^2H'^2\tau_{\parallel,RF}^2}{(\omega^2-\gamma^2B'(B'+\mu_0M_{eff}))^2+\omega^2(\gamma^2\alpha^2(2B'+\mu_0M_{eff})^2+4\alpha\gamma\tau_{\parallel,DC}(2B'+\mu_0M_{eff})\tan(\varphi))}}\hat{x} \tag{2.12}$$

$$+\omega\sqrt{\frac{\omega^2(\tau_{\parallel,RF}+\alpha\tau_{\perp,RF})^2+\gamma^2(B'+\mu_0M_{eff})^2\tau_{\perp,RF}^2}{(\omega^2-\gamma^2B'(B'+\mu_0M_{eff}))^2+\omega^2(\gamma^2\alpha^2(2B'+\mu_0M_{eff})^2+4\alpha\gamma\tau_{\parallel,DC}(2B'+\mu_0M_{eff})\tan(\varphi))}}\hat{z}$$

Note that while the DC pumped spin is proportional to the torques squared, the AC pumped spin is linear in the torques.

2.4 Mixing voltages

While the LLGS equation tells us how the magnetic moment will behave as a function of applied fields and torques, we still need a way to measure the response of the moment if we would like to determine the magnitudes of the applied torques. If the magnetic material being studied has a resistance that depends on the angle of the moment with respect to the current flow, then the RF current will mix together with the change in the resistance to generate a mixing voltage. In an amorphous or polycrystalline magnetic metal this is usually caused by the anisotropic magnetoresistance, in which the resistivity is the largest when the magnetic field is perpendicular to the current direction and has the form $\rho(\varphi)=\rho_{90^\circ}+(\rho_{0^\circ}-\rho_{90^\circ})\cos(\varphi)^2$.[57]

For any effect that causes the resistance to vary with the angle between the moment and the current, the mixing voltage is given by[58]

$$V_{mix} = \langle \delta I \cdot \delta R \rangle = \langle \delta I \cdot \left(\frac{d R}{d \varphi} \right) \cdot \delta \varphi \rangle = \langle I_{RF} \cos(\omega t) \cdot \left(\frac{d R}{d \varphi} \right) \cdot \Re(m_x(t)) \rangle \qquad 2.13$$

In general for small excitations $\Re(m_x(t))$ oscillates sinusoidally with a phase and magnitude that varies across the resonance. Only the component proportional to $\cos(\omega t)$ contributes to the mixing voltage, and using the LLGS calculation above we see that

$$\begin{aligned} V_{mix} &= I_{RF} \frac{\omega}{2\pi} \left(\frac{dR}{d\varphi} \right) \int_0^{2\pi/\omega} \cos(\omega t) \Re(m_x(t)) \, dt \\ &= \frac{I_{RF}}{2} \frac{dR}{d\varphi} \frac{\gamma \omega^2 \tau_{\perp, RF} (B' + \mu_0 M_{eff}) - \gamma^3 \tau_{\perp, RF} B' (B' + \mu_0 M_{eff})^2 - \alpha \gamma \omega^2 (2B' + \mu_0 M_{eff}) \tau_{\parallel, RF}}{(\omega^2 - \gamma^2 B' (B' + \mu_0 M_{eff}))^2 + \omega^2 (\gamma^2 \alpha^2 (2B' + \mu_0 M_{eff})^2 - 4 \alpha \gamma \tau_{\parallel, DC} (2B' + \mu_0 M_{eff}) \tan(\varphi))} \end{aligned} \qquad 2.14$$

There are other effects that can contribute to a DC mixing voltage. Taylor expanding the voltage to second order in φ and I, we see that[59]

$$\begin{aligned} V(t) = \underbrace{V_0}_{1} + \underbrace{\frac{\partial V}{\partial \varphi} \Re\left(m_x(t)\right)}_{2} + \underbrace{\frac{\partial V}{\partial I} \left(I_{RF} \cos(\omega t) \right)}_{3} + \underbrace{\frac{1}{2} \frac{\partial^2 V}{\partial \varphi^2} \left(\Re\left(m_x(t)\right)^2 \right)}_{4} \\ \underbrace{+ \frac{\partial^2 V}{\partial \varphi \, \partial I} \left(\Re\left(m_x(t)\right) I_{RF} \cos(\omega t) \right)}_{5} + \underbrace{\frac{\partial^2 V}{\partial I^2} \left(I_{RF} \cos(\omega t) \right)^2}_{6} \end{aligned} \qquad 2.15$$

In a measurement where we lock into a modulation of the RF current, the 1st term vanishes, and the 2nd and 3rd terms are purely sinusoidal at the RF frequency, and don't show up in a mixing measurement (although they could appear in a AC spin pumping measurement or similar). The

5th term is the normal mixing voltage term that is described in Formula 2.22. The 6th term depends on the non-linearity in the differential resistance, $\left(\partial^2 V / \partial I^2\right)[I_{DC}]$, and for a constant RF power scales roughly proportional to the DC current. In normal ST-FMR mixing measurements this does not contribute significantly, but for the mixing measurements with applied DC currents described in Section 2.8 it can create a large constant offset. It appears even when modulating the power since it is also proportional to $\left(I_{RF}\cos(\omega t)\right)^2$, and can lead to digital bin noise issues at large biases or for devices with strongly nonlinear differential resistance.

2.5 Inverse Spin Hall Effect-like voltages

In this section, $\hat{s}$ refers to the orientation of the spin while $\hat{j}_s$ and similar refer to the direction of the current. In the simplest model of spin relaxation in a normal metal, the spin pumped through one surface decays as a function of the distance from the interface[60]

$$j_s(z)\hat{s} = j_s^0 \hat{s} \frac{\sinh\left((t_N - z)/\lambda_{sd}\right)}{\sinh\left(t_N/\lambda_{sd}\right)} \tag{2.16}$$

This assumes that the spin relaxation in the non-magnetic material is uniform across the material, which may not be the case in topological insulators. In the case of the spin Hall effect this is converted to a perpendicular charge current density the magnitude of which also varies with distance from the surface

$$j_c^{ISHE}(z) = \theta_{\parallel} \frac{2e}{\hbar}\left(\vec{j}_s(z) \times \hat{s}\right) \tag{2.17}$$

The net charge current in a bar of width w is

$$I_{ISHE} = j_s^0 \theta_{\parallel} \frac{2e}{\hbar} \lambda_{sd} w \tanh\left(t_N / 2\lambda_{sd}\right)\left(\hat{s} \times \hat{j}_s\right) \tag{2.18}$$

If the bar is connected to a circuit with sufficiently high output impedence, this results in a voltage drop across the length of the bar. The voltage is given by

$$V_{sp} = \theta_{\parallel} e w \lambda_{sd} \frac{R}{2\pi} \tanh\left(t_N / 2\lambda_{sd}\right) \Re\left(g_{\uparrow\downarrow}^{eff}\right)\left(\vec{m}(t) \times \frac{d\vec{m}(t)}{dt}\right) \tag{2.19}$$

The easiest way to estimate the effective real component of the spin mixing conductance is from the difference in the damping coefficient of the magnetic material with and without the presence of the non-magnetic detector material[61,62]

$$g_{\uparrow\downarrow}^{eff} = \frac{4\pi M_S t_M}{g \mu_B}\left(\alpha - \alpha_0\right) \tag{2.20}$$

(In permalloy at the thicknesses we normally use in our devices, $g \approx 2$).[63]

While the full formula for $\vec{m}(t) \times \dot{\vec{m}}(t)$ is given above, its DC component can also be written in a simpler form that allows it to be easily estimated without fitting.[64]

$$\left\langle \vec{m}(t) \times \frac{d\vec{m}(t)}{dt} \right\rangle_x = \omega \phi_p^2 \sin(\varphi) \sqrt{\frac{B_{ext}}{B_{ext} + \mu_0 M_{eff}}} \tag{2.21}$$

where ϕ_p is the maximum precession angle (in the sample plane). It can be calculated using

$$\phi_p = \frac{1}{dR/d\varphi}\frac{2}{I_{RF}}\sqrt{\left(V_{mix}^{S}\right)^2+\left(V_{mix}^{A}\right)^2} \qquad 2.22$$

where V_{mix}^{S} and V_{mix}^{A} are the symmetric and antisymmetric components of the mixing voltage, which can either be determined from fitting or estimated from the net mixing voltage.

2.6 Determining spin torque conductivities and efficiencies

The spin torque conductivity is defined analogously to the electrical conductivity

$$\sigma_{S,i} = \frac{J_{S,i}\,l}{I_{RF}Z_{RF}} = \tau_i \frac{2e}{\hbar}\frac{M_S t_{mag} l}{I_{RF}Z_{RF}\gamma\cos(\varphi)} \qquad 2.23$$

where $J_{S,i}$ is in charge units, Z_{RF} is the device impedance at the driving frequency, and *l* is the length of the bar. The spin torque ratio (or spin torque efficiency) is the unitless ratio of upward-traveling spin current density to the forward-traveling charge current density in the active material

$$\theta_i = \frac{J_{S,i}}{J_C} = \frac{\sigma_{S,i}}{\sigma_{active}} = \tau_i \frac{2e}{\hbar}\frac{M_S t_{mag} l}{I_{RF}Z_{RF}\gamma\cos(\varphi)\sigma_{active}} \qquad 2.24$$

where σ_{active} is the conductivity of the active layer. Unlike the spin torque conductivity, calculating the spin torque ratio requires knowing how much of the current flows through the active layer in the device (implicitly through σ_{active}).

The expected contribution to $\sigma_{S,\perp}$ from the Oersted field flowing in the active layer of the device is

$$\sigma_{Oe} = \frac{e\mu_0 M_s t_{mag} t_{active} \sigma_{active}}{\hbar} \quad 2.25$$

and similarly the contribution to $\theta_\perp$ from the Oersted field is

$$\theta_{\perp,Oe} = \frac{e\mu_0 M_s t_{mag} t_{active}}{\hbar} \quad 2.26$$

This makes the approximation that the in-plane component of the Oersted field is constant across the device, which is a very good approximation as seen in Section 4.4. It does not include the out-of-plane component of the Oersted field, which is significant at the edges of the microstrip, but averages to zero overall.

2.7 Angular dependence of mixing and spin pumping voltages

The torques in Formula 2.14 are defined in a way that is independent of the angle between the current and the external magnetic field, $\tau_\parallel \propto \hat{m} \times (\hat{x}' \times \hat{m}) / |\hat{x}' \times \hat{m}|$ and $\tau_\perp \propto (\hat{x}' \hat{\times} \hat{m}) / |\hat{x}' \times \hat{m}|$. However, consider the torque due to a fixed upward-traveling spin current density or a constant Oersted field as the direction of the external magnetic field rotates. In the first case the resulting torque scales as $\cos(\varphi)$ due to the misalignment between the orientation of the spins, x', and the angle at which they would apply the largest torque, x. This is the origin of the $\cos(\varphi)$ term in Formulas 2.23 and 2.24. For an Oersted field, the torque similarly scales as as $\cos(\varphi)$.

The mixing voltage generated by these torques in ST-FMR is proportional to $dR/d\varphi \propto \sin(\varphi)\cos(\varphi)$, so the net angular dependence for the mixing voltage is $\cos(\varphi)^2 \sin(\varphi)$.

In DC spin pumping, the pumped spin is proportional to the torques squared, or $\cos(\varphi)^2$. The projection of that voltage on the direction of the RF current is $\sin(\varphi)$, so the next angular dependence for DC spin pumping is also $\cos(\varphi)^2\sin(\varphi)$. Because of this, these two components can not be distinguished by their angular dependence. The mixing voltages we observe agree very well with this angular dependence, as seen in Figure 2.2.

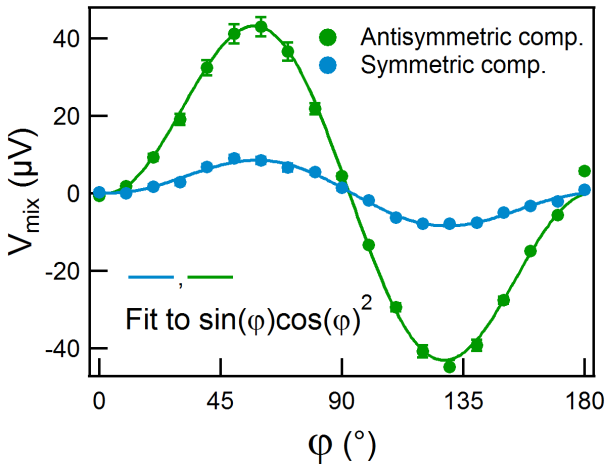

Figure 2.2. Illustration of the angular dependence of the two components of the mixing voltage in a typical device. Both the symmetric component, proportional to $\tau_{\parallel}$, and the antisymmetric component, proportional to $\tau_{\perp}$, scale as expected with angle. This data is for the same device shown in Figure 3.5.

One possible way to separate our the different contributions is to look at the voltage generated at an in-plane angle perpendicular to the direction of the RF current. The generation of the torques still scales as $\cos(\varphi)$, but to first order no voltage is generated via mixing with the AMR since there is no net current in this direction. The voltage generated by spin pumping and the ISHE does appear, and has a net angular dependence of $\cos(\varphi)^3$. However, there are several other affects that can play a role in the perpendicular voltage. If the voltage leads are not exactly perpendicular to the current direction then the normal ST-FMR signal can mix in, and AC spin

pumping generates a RF current in this direction, which can mix with the AMR into a DC signal. Nevertheless, this perpendicular voltage may be an important tool in future studies.

2.8 Mixing measurements with applied DC current

If we apply a DC current in addition to the RF current driving FMR in a bilayer device, the in-plane and out-of-plane DC torques each have a distinct effect. An in-plane torque modifies the effective damping (although it has a different field/frequency dependence than the usual damping term), and an out-of-plane DC torque acts like a small change in the external field applied to the device, as described in Formula 2.14. The circuit used in this setup is shown in Figure 2.3.

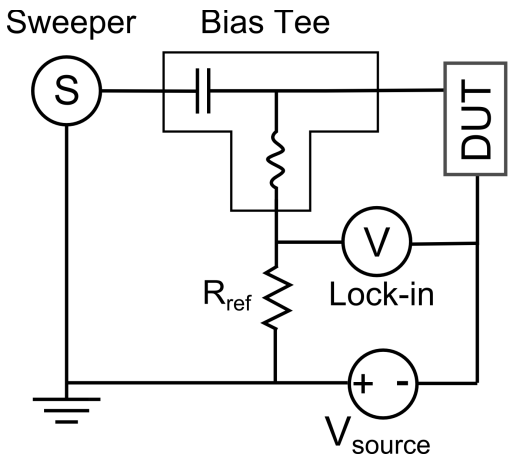

Figure 2.3. The circuit used to perform mixing measurements while also applying DC currents. The DC current applied to the device under test (DUT) is $V_{source}/(R_{ref}+R_{DUT})$.

The results of a typical measurement are shown in Figure 2.4. Note that the increase in damping due to $\tau_{\parallel,DC}$ appears as a change in the height of the resonance peak rather than a broadening of the peak at a constant height. This can clearly be seen in Formula 2.14.

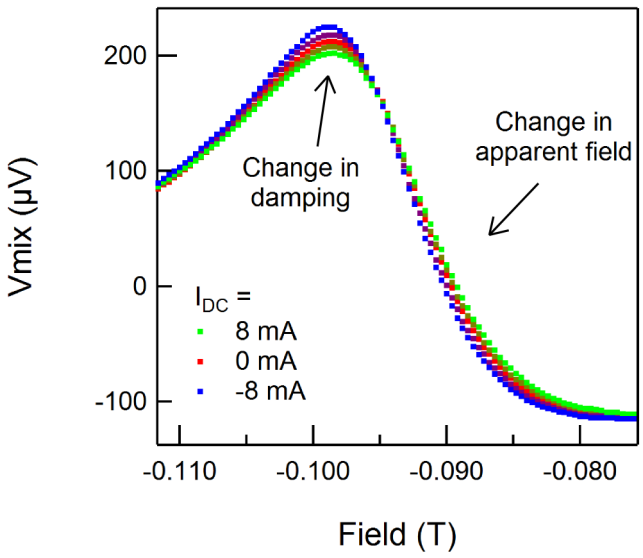

Figure 2.4. Illustration of the changes seen in the mixing voltage for applied DC torques. The in-plane DC torque modifies the damping, and the out-of-plane DC torque acts as a modification to the external field. The data shown is for a sample with 6 nm of platinum and 2 nm of permalloy at 8 GHz.

In both cases, the effect is independent of the RF torques in the device. By fitting to the mixing voltages at a range of applied DC currents we can extract the torque efficiencies of the active material without needing to know the magnitude of the RF current.

The out-of-plane DC torque modifies the external field as $B' = B - \tau_{\perp,DC}\tan(\varphi)/\gamma$, and the spin torque conductivity can be determined from

$$\frac{dB'}{dI_{DC}} = -\frac{d\tau_{\perp,DC}}{dI_{DC}}\frac{\tan(\varphi)}{\gamma} = \sigma_{S,\perp}\frac{\hbar}{2e}\frac{R_{DC}\gamma\sin(\varphi)}{M_S t_{mag} l} \qquad 2.27$$

$$\sigma_{S,\perp} = \left(\frac{dB'}{dI_{DC}}\right)\frac{2e}{\hbar}\frac{M_S t_{mag} l}{R_{DC}\sin(\varphi)} \qquad 2.28$$

Fitting to Formula 2.14 gives the in-plane DC torque directly, from which we can similarly

calculate the spin torque conductivity from the slope

$$\sigma_{S,\parallel}=\left(\frac{d\,\tau_{\parallel,DC}}{dI_{DC}}\right)\frac{2e}{\hbar}\frac{M_S t_{mag} l}{R_{DC}\gamma\cos(\varphi)} \tag{2.29}$$

2.9 Determining RF currents

We use a calibrated vector network analyzer to determine the RF characteristics of our system. First, we perform an enhanced response calibration[65] using a 50 Ohm standard 2.4 mm calibration kit, and then measure the transmission coefficient (S_{21}) of our DC block, cables and bias tee as a function of frequency in our measurement range. We then attach the network analyzer to our RF probes and use a 50 Ohm standard calibration kit from Cascade to make a one-port short-load-open calibration, and then measure the voltage reflection coefficient of our device (S_{11}).

The network analyzer reports both values in dB, and while S_{ij} represents a voltage ratio, its value in dB is written as a power. The scalar reflection coefficient is then

$$\Gamma=Sgn(Z_{RF}-Z_0)\,10^{S_{11}/20}=\frac{Z_{RF}-Z_0}{Z_{RF}+Z_0} \tag{2.30}$$

where Z_0 is the characteristic impedance and Z_{RF} is the device impedance. Γ is negative when the device impedance is less than the transmission line impedance. In our devices Z_{RF} is equal to the device's DC resistance to within a few percent which means that Γ is constant over the range of frequencies we study. The power produced by our RF generator is set in dBm which is defined with respect to 1 mW. The power and voltage input into our RF network by the signal

generator are given by

$$P_{sg} = 1\,mW \cdot 10^{P/10} \quad , \quad V_{sg,a} = \sqrt{2 \cdot 1\,mW \cdot 10^{P/10} Z_0} \tag{2.31}$$

where the voltage is written as the amplitude of the wave, not the RMS value. By the time the signal reaches the device it has been attenuated such that

$$P_{at\,dev} = 1\,mW \cdot 10^{(P+S21)/10} \quad , \quad V_{at\,dev,a} = \sqrt{2 \cdot 1\,mW \cdot 10^{(P+S21)/10} Z_0} \tag{2.32}$$

Not all of this power is absorbed by the device. Some is reflected back into the network, and ignoring higher-order mismatch effects, it is absorbed. The voltage of the reflected wave is $V_{at\,dev,a,refl} = \Gamma \cdot V_{at\,dev,a}$. At the interface with the device the voltages and the currents must be continuous. This implies that the voltage which actually makes it into the device is

$$V_{dev,a} = \sqrt{2 \cdot 1\,mW \cdot 10^{(P+S21)/10} Z_0}\,(1+\Gamma) = \sqrt{2 \cdot 1\,mW \cdot 10^{(P+S21)/10} Z_0}\left(\frac{2 Z_{RF}}{Z_{RF}+Z_0}\right) \tag{2.33}$$

In the case that the impedance of the device is higher than the line impedance, the voltage in the device is actually larger than the voltage incident on it from the line. This does not violate the conservation of power since the power delivered to the device is

$$P_{dev} = \frac{\left(V_{at\,dev,a}(1+\Gamma)\right)^2}{2 Z_{RF}} = V^2_{at\,dev,a}\left(1+\frac{Z_{RF}-Z_0}{Z_{RF}+Z_0}\right)^2 \frac{1}{2 Z_{RF}} = V^2_{at\,dev,a}\frac{2 Z_{RF}}{(Z_{RF}+Z_0)^2} \tag{2.34}$$

which is always smaller than or equal to the power incident on it, $V^2_{at\,dev,a}/(2 Z_0)$. The RF

current in the device can then be found by dividing by the device impedance

$$I_{dev,a} = \sqrt{2 \cdot 1\,mW \cdot 10^{(P+S21)/10} Z_0} \left(\frac{2}{Z_{RF} + Z_0} \right) \tag{2.35}$$

An alternate way to calculate the RF current is using the power transmission coefficient[66] which is

$$1 - |\Gamma|^2 = \frac{4 Z_{RF} Z_0}{(Z_{RF} + Z_0)^2} \tag{2.36}$$

We normally modulate the amplitude of the RF signal and measure the resulting mixing voltage using a lock-in amplifier. When amplitude modulation (AM) is turned on with a modulation index (referred to as modulation depth on Agilent signal generators) of 100%, the voltage output from the signal generator varies from zero to twice the voltage corresponding to the power setpoint. This means that turning on AM actually increases the time-averaged power output, and the power in dBm is increased by $10\log(4)/\log(10) \approx 6.02$ dB. The voltage is being modulated rather than the power, so the peak RF current and voltage in the device are just twice what they would be with AM turned off.

When AM is enabled the mixing voltage varies from zero to some peak value. Our lock-in amplifier ignores the DC offset and reports the RMS voltage from the center of the waveform. This means that the actual peak mixing voltage is $2\sqrt{2}$ times larger than what we measure with the lock-in, as shown schematically in Figure 2.5.

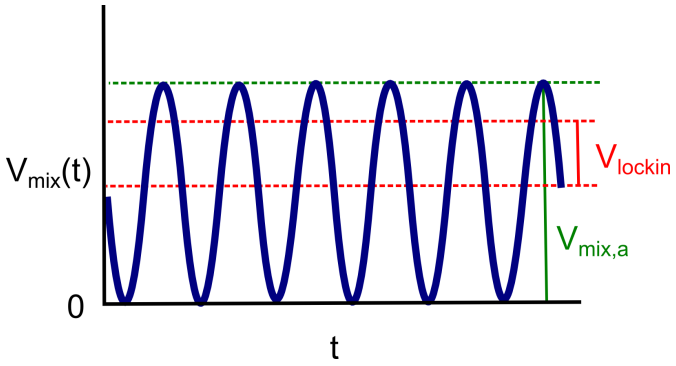

Figure 2.5. Illustration of the mixing voltage signal seen by the lock-in amplifier for amplitude-modulated ST-FMR. The mixing voltage varies from zero to a value $V_{mix,a}$ *which is* $2\sqrt{2}$ *larger than the RMS value reported by the lock-in.*

3. ST-FMR Measurements on Bismuth Selenide

This chapter is closely based on work published as A.R. Mellnik *et al*. Spin-transfer torque generated by a topological insulator, *Nature* **511**, 449-451 (2014).

Now that we know how spin torques affect magnetic films, we can characterize spin torques generated by a topological insulator, as motivated in Section 1.7. We give a more thorough discussion of the proposed effect and discuss the specifics of how we make samples, characterize them, and make measurements. Using normal ST-FMR we find that both the in-plane and out-of-plane spin torque ratios are at least of order ~ 1, and using ST-FMR with applied DC currents we find that the out-of-plane spin torque ratio is at least ~ 3, which are several times larger than any values previously measured at room temperature. Lastly, we discuss possible contributions from spin pumping, and compare our findings to theoretical calculations performed by the Kim group at Cornell.

3.1 Background and motivation

Topological insulators have surface states in which the spins of carriers are locked perpendicular to their momentum. In bismuth selenide, the prototypical topological insulator,† these states form a Dirac cone that traverses the bulk gap. The intersection of the Fermi surface with the surface states forms a ring in which the orientation of the spins winds around in a circle. In the absence of an electric field the integrated states have zero total spin (although they do have a *non-transport* spin current as detailed by Peshin & MacDonald[44] and Rashba[67]). In the presence of an electric field, the surface states shift in momentum space leading to more of one direction of spin and less of the other, leading to a net spin accumulation, as shown schematically in Figure 3.1.

† As-grown bismuth selenide is normally a bulk semimetal, but the protected surface states are still present.

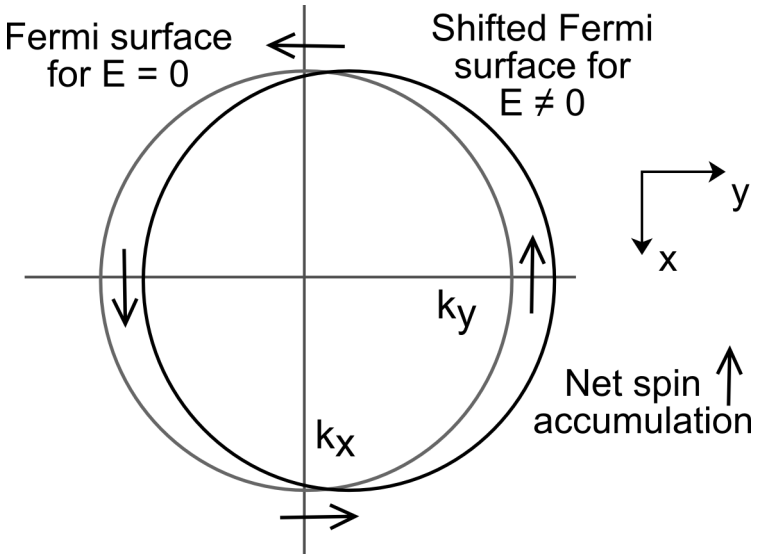

Figure 3.1. Schematic diagram of a topological insulator surface state. When an electric field is applies more spins of one direction and less of the other are occupied, leading to a net non-equilibrium spin accumulation.

If this spin accumulation is allowed to interact with an adjacent ferromagnetic layer, it can transfer angular momentum and apply a spin torque. This effect does not require that the Fermi level fall near the Dirac point and is expected to occur even in the presence of bulk states. It is analogous to the Rashba-Edelstein effect in non-topological materials.[37]

3.2 Methods

We started with ~ 8 nm bismuth selenide thin films grown with molecular beam epitaxy by our collaborators in Nitin Samarth's group at Penn State University. The growth process is detailed in the paper[64] and in other publications by the Samarth group. After growth the films were capped with a ~4 nm layer of amorphous selenium to protect the surface. The films were then shipped to Cornell, where we loaded them into our six-gun UHV magnetron sputtering system. We heated the samples to a nominal temperature of 240 C for one hour to desorb the selenium cap and then allowed the samples to cool to room temperature. We then sputtered the desired

thickness of permalloy at 2.5 mTorr followed by 2 nm of metallic aluminum. Prior to removing the sample from the vacuum system, we exposed it to a dry oxygen/nitrogen mixture to oxidize the aluminum to create a protective layer.

The room-temperature carrier density of our bismuth selenide films with the selenium capping layer is 2.1×10^{13} cm^{-2}, and 9.4×10^{13} cm^{-2} with the aluminum oxide capping layer. The conductivity of the aluminum-capped bismuth selenide film was $\sim 5.7 \times 10^{4}$ Ω^{-1} m^{-1}. Other groups have studied[68] the band-bending of bismuth selenide due to an adjacent metallic layer, and found that these result in a maximal surface charge density of 5×10^{13} cm^{-2}. Because of this, we estimate that the conductivity of our bismuth selenide layers should be similar when the aluminum oxide is replaced with permalloy. The resistivity of the permalloy changes with thickness due to the roughness of the bismuth selenide underlayer, and is 71.7 μΩ cm for a nominally 8 nm layer and 45.9 μΩ cm for a nominally 16 nm layer.

We fabricated microstrip devices using a standard photolithographic process (described in the Appendix) at the Cornell Nanoscale Science & Technology Facility (CNF). We etch the microstrips using the Buhrman group's endpoint detection ion mill, and deposit symmetric ground-signal-ground contacts with 3 nm titanium / 150 nm platinum in a CNF sputtering system. The active regions of our devices range from 10–80 μm long and 2.5–24 μm wide. A typical device is shown in Figure 3.2.

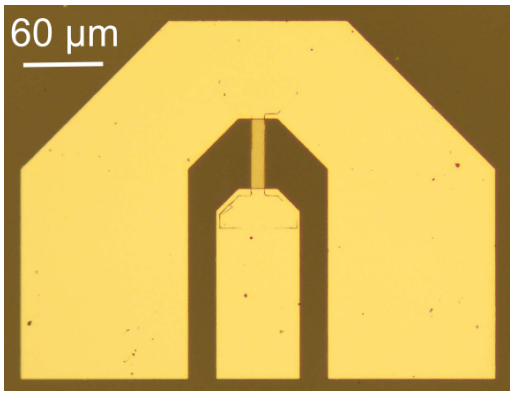

Figure 3.2. A typical ST-FMR device consists of a bilayer microstrip with attached ground-signal-ground RF leads. The symmetric arrangement of the leads prevents the current flowing in the leads from applying a net Oersted torque to the magnetic layer of the microstrip.

We used the Cornell Center for Materials Research (CCMR) vibrating sample magnetometer setup to measure the saturation magnetization of the bilayers. For 8 nm bismuth selenide / 16 nm permalloy films $M_S t_{mag}$ = 14.2 mA and for the 8 nm bismuth selenide / 8 nm permalloy films $M_S t_{mag}$ = 7.1 mA. $\mu_0 M_S$ = 1.11 ± 0.2 T in both cases which agrees well with the values of $\mu_0 M_{eff}$ we measure with FMR.

We characterize the anisotropic magnetoresistance of the devices using the CCMR projected field measurement station. We apply a 0.07 T in-plane field to the sample, and rotate its direction while performing a four-terminal resistance measurement on each device. A typical measurement is shown in Figure 3.3.

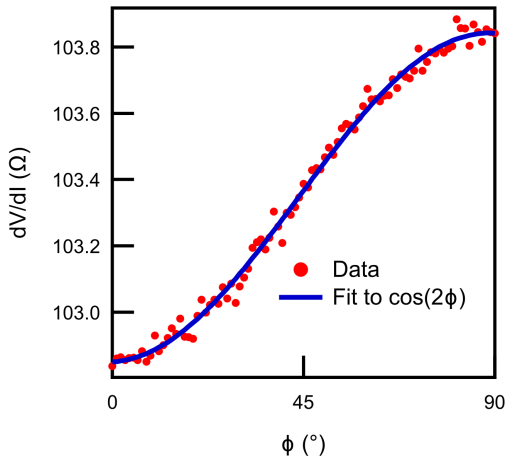

Figure 3.3. A typical anisotropic magnetoresistance calibration for a 50 μm × 15 μm device with 16 nm of permalloy.

We perform a linear fit in the region near $\varphi = 45°$ to determine $dR/d\varphi$. This value does not change appreciably for applied fields above ~ 0.02 T.

Next, we determine S_{11} for each device and S_{21} for our measurement setup, as discussed in Section 2.9. For each device, we use a script written in Igor Pro to calculate the power we need to source at each frequency to have a set power absorbed by the device.

We perform our ST-FMR measurements using the CCMR table-top probe station. We use an Agilent 20 GHz signal generator set in AM mode to source the RF excitation, and use a lock-in amplifier locked to the modulation frequency of the signal generator to measure the mixing voltage as we sweep the external magnetic field at 45° from the current direction. A diagram of the measurement setup is shown in Figure 3.4.

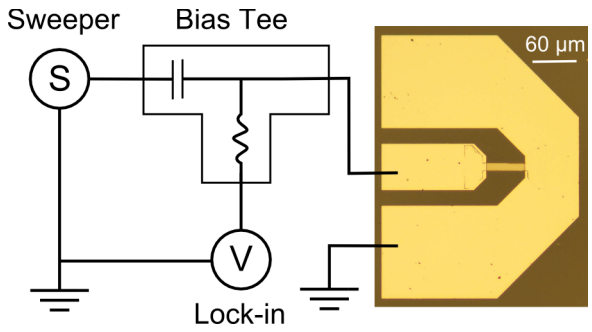

Figure 3.4. Simplified diagram of our measurement setup. Contacts are made to the device using ground-signal-ground probes in the probe station. Not shown is a DC block on the output of the signal generator to protect it from possible damage due to DC voltages.

We sweep the applied field from -0.15 T to 0.15 T in two segments so that the field value is always ramping toward zero field while measuring. This is intended to reduce any hysteretic effects in our device or magnetic probe station, but may not be necessary. A typical mixing voltage curve is shown in Figure 3.5.

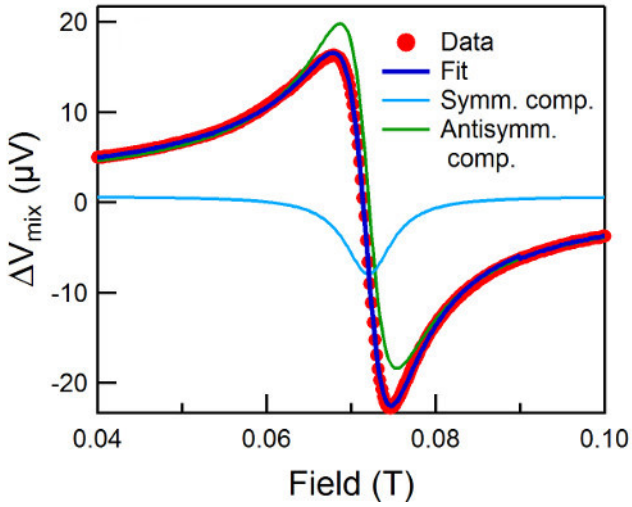

Figure 3.5. A typical mixing voltage signal at resonance, showing the fit and its two components; a symmetric component due to $\tau_{\parallel}$ and an antisymmetric component due to $\tau_{\perp}$. The measurement shown is for a 50 μm × 15 μm, 8 nm bismuth selenide / 16 nm permalloy device at 8 GHz. The peak microwave power absorbed by the device is 14.2 dBm and I_{RF} = 22 ± 3 mA. The measured torques per unit moment were $\tau_{\parallel}$ = (3.6 ± 0.4) × 10^{-5} T and $\tau_{\perp}$ = (4.6 ± 0.5) × 10^{-5} T in field units.

For each thickness of permalloy we measured three different devices between 6 and 10 GHz at 0.5 GHz intervals. There was ~ 20% variation in the calculated spin torque conductances between devices with the same thickness of permalloy, but no systematic dependence on device dimensions or frequency.

3.3 Spin torque conductivities

Averaging over multiple devices with 8 nm bismuth selenide and 8 nm permalloy we calculated the spin torque conductivities, using Formula 2.23, as $\sigma_{S,\parallel} = (3.0 \pm 0.5) \times 10^4 \ \hbar/2e\ \Omega^{-1}m^{-1}$ and $\sigma_{S,\perp} = (2.5 \pm 0.4) \times 10^4 \ \hbar/2e\ \Omega^{-1}m^{-1}$. Averaging over devices with 16 nm permalloy we find $\sigma_{S,\parallel} = (5.5 \pm 0.8) \times 10^4 \ \hbar/2e\ \Omega^{-1}m^{-1}$ and $\sigma_{S,\perp} = (6.7 \pm 1.0) \times 10^4 \ \hbar/2e\ \Omega^{-1}m^{-1}$. These values are comparable to those measured in heavy metal systems which have much higher charge conductivities.[29,33,69,70] This indicates that per unit charge current density, bismuth selenide will likely be much more efficient at generating spin currents. The value that we determine for $\sigma_{S,\perp}$ is several times larger than the expected contribution from the Oersted field calculated using Formula 2.25, $\sigma_{S,Oe} \approx 6.1 \times 10^3 \ \hbar/2e\ \Omega^{-1}m^{-1}$ for the devices with 8 nm permalloy, and $\sigma_{S,Oe} \approx 1.2 \times 10^4 \ \hbar/2e\ \Omega^{-1}m^{-1}$ for the devices with 16 nm permalloy.

3.4 Spin torque efficiencies

For spin generating applications, the appropriate figures of merit are the spin torque efficiencies (or spin torque ratios) as defined in Formula 2.24. This is more challenging to measure because it requires determining how much current flows through the bismuth selenide active layer, and not just the voltage across both components of the bilayer. Based on our discussions of the carrier density and proximity doping in Section 3.2, we assume that the conductivity of our bismuth selenide films in the bilayers are equal to or less than the conductivity of the films

capped with aluminum oxide. Using this value, we calculate lower bounds for the in-plane spin torque ratios of $\theta_{\parallel} \geq 0.5$ based on devices with 8 nm permalloy and $\theta_{\parallel} \geq 1.0$ based on devices with 16 nm permalloy. For the out-of-plane spin torque efficiencies, we find $\theta_{\perp} \geq 0.4$ based on devices with 8 nm permalloy and $\theta_{\perp} \geq 1.1$ based on devices with 16 nm permalloy.

3.5 DC-current mixing measurements

We also performed DC-current mixing measurements of the type discussed in Section 2.8. While we could observe significant modifications of the damping with DC current, we were unable to determine a value for $\theta_{\parallel}$ because this linewidth did not scale linearly with frequency as expected, nor does the change in linewidth with DC current have the expected frequency dependence. The observed relationship between linewidth and frequency is shown in Figure 3.6.

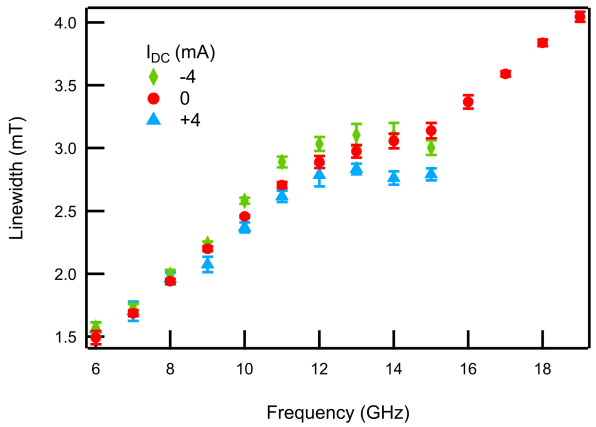

Figure 3.6. Linewidth verses frequency as a function of DC current for a 50 μm × 10 μm device with 8 nm of bismuth selenide and 16 nm of permalloy. The linewidth is only linear with frequency below 12 GHz, and the change in linewidth with current does not obey the form expected from Formula 2.14.

We do, however, observe the expected change in resonant frequency due to $\tau_{\perp,DC}$. Figure 3.7 shows the mixing voltage near a resonance for a typical device as a function of applied DC current. The shift in apparent field is most apparent directly at the resonance field where the

value of the mixing voltage is changing rapidly.

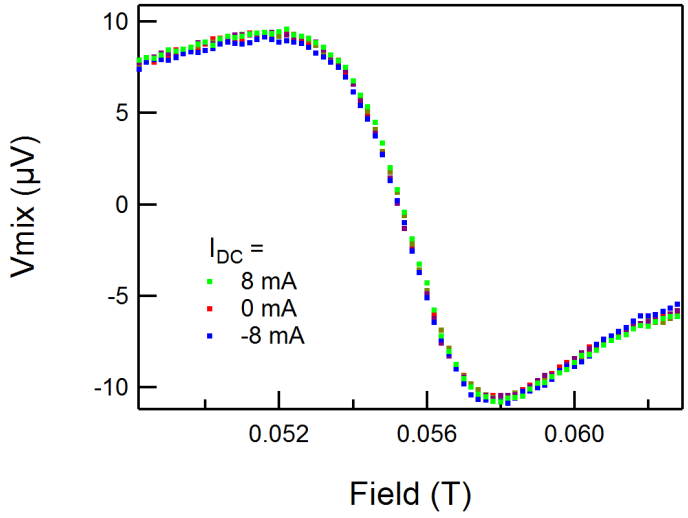

Figure 3.7. Mixing voltage verses applied field as a function of DC current for a 50 μm × 15 μm device with 8 nm of bismuth selenide and 16 nm of permalloy at 7 GHz. To determine the DC torque we simultaneously fit to the mixing voltages at frequencies between 6 and 10 GHz at 1 GHz intervals to determine the average shift per applied DC current.

By fitting to the mixing voltages at a range of frequencies we can determine the shift in apparent field verses applied DC current. Data for a typical device is shown in Figure 3.8.

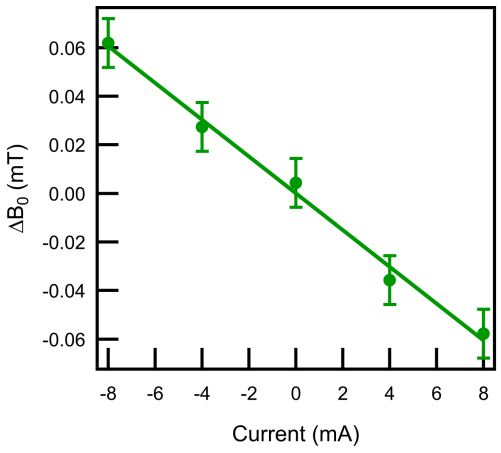

Figure 3.8. Change in apparent field as a function of applied DC current for a 50 μm × 15 μm device with 8 nm of bismuth selenide and 16 nm of permalloy. Each data point represents an average shift over frequencies between 6 and 10 GHz.

We perform linear fits to the change in field verses current and determine that dB'/dI_{DC} = (7.2 ± 0.5) × 10^{-3} T/A for the device shown in Figure 3.8. From this value we calculate, using Formula 2.28, that $\sigma_{S,\perp}$ = (2.2 ± 0.3) × 10^5 $\hbar/2e\ \Omega^{-1}m^{-1}$. Averaging over multiple devices we find that $\sigma_{S,\perp}$ = (2.2 ± 0.6) × 10^5 $\hbar/2e\ \Omega^{-1}m^{-1}$ in devices with 16 nm of permalloy. This value is ~ 3 times larger than what we measured using the standard ST-FMR technique, which suggests that we somewhat overestimate the total RF current in our devices.

3.6 Contributions from spin pumping

One possible artifact in this measurement is that spin pumping, combined with the inverse Edelstein effect (analogous to the inverse spin Hall effect), can also generate a symmetric voltage signal near resonance as described in Formula 2.19. Normally, $\Re(g^{eff}_{\uparrow\downarrow})$ is measured by comparing the change in damping with and without the spin sink material, but this is not possible in our system since the linewidth of the permalloy is also increased by the roughness of the bismuth selenide verses other substrates. Because of this, we use the value measured in platinum/permalloy bilayers, $\Re(g^{eff}_{\uparrow\downarrow})$ ≈ 2 × 10^5 m^{-2} as an upper bound, since bismuth selenide is much more resistive and unlikely to have a higher spin mixing conductance. We similarly note that the spin diffusion length in the bismuth selenide can not be longer than half the thickness of the bismuth selenide film. Using Formula 2.22 we calculate that the maximum cone angle of precession for the measurement shown in Figure 3.5 is φ_p ≈ 0.013. From this and from our estimates for $\theta_\parallel$ we find that spin pumping should contribute at most $V_{sp} \leq 5$ μV, which is negligible compared the total mixing voltage. Because of this, it is safe to say that either spin pumping does not contribute significantly to this measurement, or if it does, $\theta_\parallel$ is even larger than we measure above.

3.7 Comparison to theoretical calculations

Our collaborators in the Kim group at Cornell calculated the expected non-equilibrium spin accumulation on the surface of bismuth selenide due to both the topologically protected surface states as well as the Rashba-split two-dimensional electron gas states that are also seen at the interface.[71–73] The calculation is described in detail in a preprint[47] and also in the supplementary info of our *Nature* paper.[64] In bismuth selenide, the TI surface states and the Rashba-split states are expected to generate torques of opposite sign, and the Rashba-based torque from the highest-momentum sub-band should be partially canceled by the next-highest momentum sub-band. The sign of torque that we observe in our devices is consistent with the direction calculated by the surface states, which suggest that they are the primary mechanism for generating spin torque. In their model, the spin torque efficiencies are

$$\theta_{\parallel} + i\theta_{\perp} = \frac{\sqrt{2}}{2}\frac{D}{v_F k}\left(\frac{1}{\lambda_{\phi}^2} - \frac{i}{\lambda_j^2}\right) \tag{3.1}$$

where D is the diffusion constant, v_F is the Fermi velocity, λ_{ϕ} is the spin decoherence length and λ_j is the spin precession length. Using typical values for bismuth selenide at room temperature, this suggests that both $\theta_{\parallel}$ and $\theta_{\perp}$ should be of order 1, which agrees well with our measured values.

4. The Magneto-Optic Kerr Effect

In Chapter 2 we focused on ways to measure spin torque electronically, and in Chapter 3 we saw that these work well to study bilayers involving a metallic ferromagnet. However, when paired with a resistive active layer such as bismuth selenide, these magnetic layers shunt most of the applied current away from the active layer. We saw that bismuth selenide is very efficient at generating spin torques per amount of current flowing through it, but in the devices studied in Chapter 3 it was not efficient per net current flowing through the bilayer. In order to apply the largest possible spin torques per net electrical current in a bilayer, we would ideally use an insulating ferromagnetic layer, so that all of the current flows through the active layer. Insulating ferromagnetic layers come with their own set of challenges, and it may not be practical to study their response electronically.

In this chapter we discuss a second possibility for measuring spin torques which is amendable to both metallic and insulating ferromagnetic layers using the magneto-optic Kerr effect. We give a brief overview of this effect, and work through a simple experimental geometry. We discuss a method recently developed by the Xiao and Lorenz groups at the University of Delaware for measuring spin torques using the magneto-optic Kerr effect, and also quadratic effects which can play an important role in some materials.

4.1 MOKE background and theory

In 1877, John Kerr discovered that light reflecting off a magnetic surface would have its polarization modified depending on the orientation of the magnetic field on the surface.[74] This effect, now known as the *magneto-optic Kerr effect* (MOKE, also the surface magneto-optic Kerr effect SMOKE), is the reflection-analog of the Faraday effect, in which the polarization of light

rotates as it passes through a magnetic medium.[75]

To first order, MOKE can be described by adding off-diagonal terms to the dielectric tensor. The dielectric tensor has the form[76]

$$\varepsilon = \begin{pmatrix} \varepsilon_{xx} & \varepsilon_{xy} & \varepsilon_{xz} \\ -\varepsilon_{xy} & \varepsilon_{yy} & \varepsilon_{yz} \\ -\varepsilon_{xz} & -\varepsilon_{yz} & \varepsilon_{zz} \end{pmatrix} = n_0^2 \begin{pmatrix} 1 & -iQ_z & iQ_y \\ iQ_z & 1 & -iQ_x \\ -iQ_y & iQ_x & 1 \end{pmatrix} \qquad 4.1$$

where $\vec{Q}$, the Voigt vector, characterizes the magneto-optic response of the system. For light propagating along a vector $\hat{k}$, the eigenmodes are for left- and right-circularly polarized light with refraction indices $n_{r,l} \approx n_0(1 \pm \vec{Q} \cdot \hat{k}/2)$. Linearly polarized light is a superposition of the two eigenmodes, and when reflected, the difference in refraction indices leads to a slightly different mixture of the eigenmodes, or elliptically polarized light.

Of particular interest is the matrix T that relates the *s* and *p* components (electric field perpendicular or parallel to the plane of incidence respectively) of the incident and reflected beams. In a multilayer system where the electric fields in the first and final layer are[76,77]

$$P_i = \begin{pmatrix} E_s^i \\ E_p^i \\ E_s^r \\ E_p^r \end{pmatrix} = \begin{pmatrix} E_s^i \\ E_p^i \\ r_{ss}E_s^i + r_{sp}E_p^i \\ r_{ps}E_s^i + r_{pp}E_p^i \end{pmatrix} \quad , \quad P_f = \begin{pmatrix} E_s^i \\ E_p^i \\ 0 \\ 0 \end{pmatrix} = \begin{pmatrix} t_{ss}E_s^i + t_{sp}E_p^i \\ t_{ps}E_s^i + t_{pp}E_p^i \\ 0 \\ 0 \end{pmatrix} \qquad 4.2$$

and $r_{jk}(t_{jk})$ is the ratio of the reflected (transmitted) electric field in polarization *j* to the incident electric field in polarization *k*. The matrix T is then defined by $P_i = T P_f$, but only

parts of this 4×4 matrix are relevant to experiments. If we divide it up into 2×2 blocks

$$T=\begin{pmatrix} G & H \\ I & J \end{pmatrix} \tag{4.3}$$

then all the important information is contained in G and I. In particular

$$G^{-1}=\begin{pmatrix} t_{ss} & t_{sp} \\ t_{ps} & t_{pp} \end{pmatrix} \quad , \quad I\,G^{-1}=\begin{pmatrix} r_{ss} & r_{sp} \\ r_{ps} & r_{pp} \end{pmatrix} \tag{4.4}$$

In a thin-film multilayer system where each layer is much thinner than the optical wavelength, these components can be solved for in terms of the indices of refraction, thicknesses, and Voigt vectors of the component layers (see for example reference [77]). The rotation and ellipticity for incident *s*-polarized light are then

$$\phi=\phi_s^{rot}+i\,\phi_s^{ellip}=\frac{r_{ps}}{r_{ss}} \tag{4.5}$$

and similarly for a *p*-polarized beam. If the light is incident on the surface at a normal angle and the rotation is small, we can calculate the rotation and ellipticity in terms of the two indicies of refraction as[78]

$$\phi\approx i\,\frac{(n_r-n_l)n_0}{n_r n_l-n_0^2}=\frac{-\varepsilon_{xy}\varepsilon_0}{\sqrt{\varepsilon_{xx}}(\varepsilon_0-\varepsilon_{xx})} \tag{4.6}$$

Using the relationship between the dielectric and conductivity tensors $\varepsilon_{ij}(\omega)=\delta_{ij}+i\,\sigma_{ij}(\omega)/\omega$ we can express this in terms of the conductivity tensor components as

$$\phi \approx \frac{-\sigma_{xy}}{\sigma_{xx}\sqrt{1+\frac{i}{\omega}\sigma_{xx}}} \qquad 4.7$$

and since σ_{xy} is a function of B_z and has the same parity, this can be used to determine the z component of the moment. In practice, it's very difficult to determine the actual magnitude/direction of the moment from MOKE, but proportional changes can easily be observed.

4.2 Measurement geometries and a simple MOKE measurement

From our calculation in Section 4.1 we see that to first order for light incident at a normal angle, the Kerr effect signal is proportional to the out-of-plane component of the moment. This measurement geometry is know as perpendicular-MOKE or PMOKE. The dielectric tensor in Formula 4.1 then simplifies to

$$\varepsilon = \begin{pmatrix} \varepsilon_{xx} & \varepsilon_{xy} & 0 \\ -\varepsilon_{xy} & \varepsilon_{yy} & 0 \\ 0 & 0 & \varepsilon_{zz} \end{pmatrix} = n_0^2 \begin{pmatrix} 1 & -iQ & 0 \\ iQ & 1 & 0 \\ 0 & 0 & 1 \end{pmatrix} \qquad 4.8$$

and the eigenmodes are again circularly polarized with $\varepsilon_{r,l} = n_0^2(1 \pm Q)$.

Performing a similar analysis for a beam at a non-normal angle to the surface introduces several other effects. To first order, the Kerr signal is proportional to the in-plane component of the moment parallel to the plane of the beam (longitudinal-MOKE) as well as some residual PMOKE signal. There is also a signal from the transverse-MOKE† effect which causes a

† Also confusingly known as as transversal-MOKE.

different reflection amplitude for *s*- and *p*-polarized light that is proportional to the component of the moment which is perpendicular to the plane of the beam. The three geometries are shown in Figure 4.1.

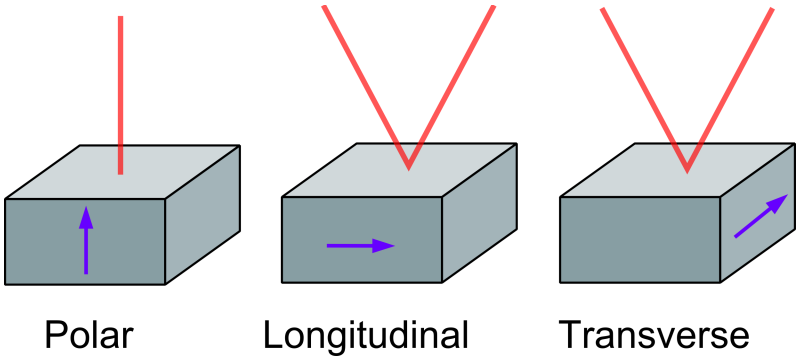

Figure 4.1. Illustration of the three most commonly used MOKE geometries, after reference [79] *(although this canonical figure appears in almost every review written on MOKE). The orientation of the magnetic moment is shown in purple. To first order, polar MOKE is only sensitive to the out-of-plane component of the moment, while the other two geometries measure a signal that is proportional to all three components of the moment.*

For a material with an out-of-plane moment, the simplest possible measurement is to apply light in the PMOKE geometry so that the two other effects vanish.

A simple PMOKE measurement geometry using a differential photodiode detector is shown in Figure 4.2.

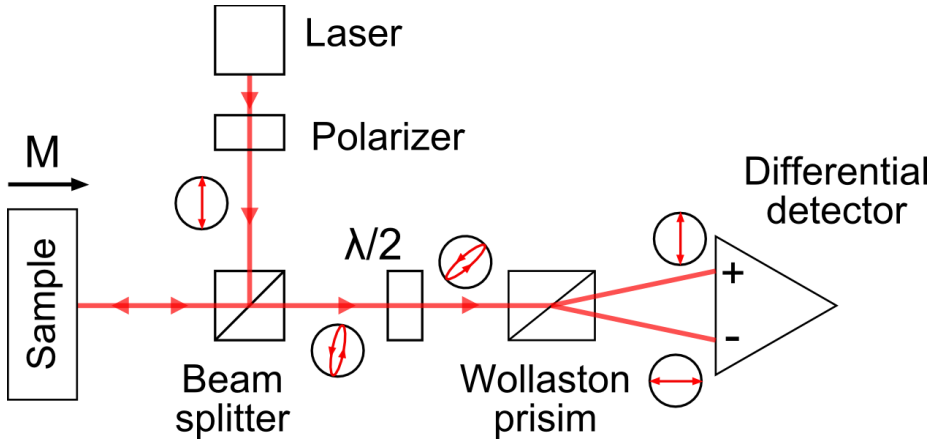

Figure 4.2. A simple MOKE measurement in the polar geometry. A linearly-polarized laser beam is directed on the surface of the sample at a normal angle after passing through a non-polarizing beam splitter. The resulting beam is slightly rotated and elliptical. A half-wave plate is used to rotate the polarization by 45°, and a Wollaston prism splits the beam into nearly-equal s *and* p *components. A differential photodiode detector measures the difference in intensity between the two components.*

The state of the laser polarization in this experiment can be described using the Jones matrix formulation, which describes the beam state in the basis of its *s* and *p* components.[80] The initial beam after the polarizer is fully polarized

$$\vec{E}_{initial} = \begin{pmatrix} 1 \\ 0 \end{pmatrix} \tag{4.9}$$

The effect of reflection off the sample surface is given by applying $I\,G^{-1}$ as defined in Formula 4.4

$$\vec{E}_{after\ sample} = I\,G^{-1}\,\vec{E}_{initial} = \begin{pmatrix} r_{ss} & r_{sp} \\ r_{ps} & r_{pp} \end{pmatrix} \begin{pmatrix} 1 \\ 0 \end{pmatrix} = \begin{pmatrix} r_{ss} \\ r_{ps} \end{pmatrix} \tag{4.10}$$

and after rotation of the polarization by the half-wave plate oriented with fast-axis an angle $\alpha = \pi/8$ from the *s* direction

$$\vec{E}_{before\ detector} = \Lambda \vec{E}_{after\ sample} = \begin{pmatrix} \cos(2\alpha) & \sin(2\alpha) \\ \sin(2\alpha) & -\cos(2\alpha) \end{pmatrix} \begin{pmatrix} r_{ss} \\ r_{ps} \end{pmatrix} = \frac{1}{\sqrt{2}} \begin{pmatrix} r_{ss} + r_{ps} \\ r_{ss} - r_{ps} \end{pmatrix} \quad 4.11$$

The split photodetector outputs a voltage proportional to the difference in power between each side, and the power is proportional to the magnitude of the electric field squared. The voltage signal is the proportional to

$$V_{detector} \propto \left(r_{ss} + r_{ps}\right)^2 - \left(r_{ss} - r_{ps}\right)^2 = r_{ss}^2 \left(\left(1 + \frac{r_{ps}}{r_{ss}}\right) - \left(1 - \frac{r_{ps}}{r_{ss}}\right)^2 \right) \approx 4\, r_{ps}\, r_{ss} \quad 4.12$$

The non-polarization term r_{ss} is much larger than r_{ps} and largely-independent of the magnetization state of the sample, and to good approximation the voltage seen at the detector is linearly proportional to the Kerr rotation ϕ_s^{rot}.

4.3 Quadratic MOKE effects

In PMOKE, the optical response and the Kerr rotation are both linear in the magnetization, *M*. However, in certain materials, there are also effects that are proportional to M^2 that can contribute significantly. We refer to these generally as *quadratic MOKE effects*, although somewhat confusingly, QMOKE refers to one specific effect discussed below. The components of the dielectric tensor described in Formula 4.1 can be written in terms of their dependence on *M* as[81–83]

$$\varepsilon_{ij} = \varepsilon_{ij}^0 + K_{ijk} M_k + G_{ijkl} M_k M_l + \ldots \quad 4.13$$

In a magnetic material many of these coefficients are redundant, and including the symmetry

considerations already shown in Formula 4.1 we have[83]

$$\varepsilon_{ij}^{(0)} = \varepsilon_{ji}^{(0)} \quad , \quad K_{ijk} = -K_{jik} \quad , \quad K_{iij} = 0 \quad , \quad G_{ijkl} = G_{jikl} = G_{jilk} = G_{ijlk} \tag{4.14}$$

In crystalline materials materials the number of coefficients can be further reduced by symmetry arguments.[82]

The first type of quadratic MOKE effect is known specifically as QMOKE, which corresponds to components of the dielectric tensor of the form G_{ijkl} where $i \neq j$. This effect modifies the off-diagonal elements of the dielectric tensor, the same elements that host the normal MOKE effect. The second type of quadratic effect is magnetic linear dichroism (MLD, also known as the Voigt effect in gases and the Cotton-Mouton effect in liquids) which corresponds to the on-diagonal elements of the form G_{ijkl} where $i = j$ and where $G_{aakl} \neq G_{bbkl}$ for $a \neq b$. In MLD, the difference in on-diagonal elements means that there are different reflection coefficients for light depending on its polarization.

The different MOKE effects each have magneto-conductive analogs,[82] as can be seen in the simple relationship between the dielectric tensor and the conductivity tensor in Formula 4.7. The linear MOKE effect with its off-diagonal terms in the dielectric tensor is the optical equivalent to the normal Hall effect, which depends on off-diagonal terms linear in M in the magnetoconductivity tensor. QMOKE corresponds to the longitudinal Hall effect, which depends on off-diagonal terms quadratic in M.[84] MLD is analogous to the anisotropic magnetoresistance and the planar Hall effect in that both depend on the difference between on-diagonal terms which are quadratic in M. This suggests that materials with significant AMR may

also exhibit large MLD, as we will see in Chapter 5.

Even if the expected components of K and G can not be calculated analytically for a given material, their contributions are fortunately easy to separate out in practice. Due to the symmetry considerations above, the linear PMOKE signal must be independent of the angle between the direction of the in-plane component of the moment and the polarization of the incident beam. However, any signal due to MLD will depend on the polarization of the incident beam due to the difference in on-axis elements of the dielectric tensor. Similarly, any QMOKE signal will depend on the polarization of the incident beam since the off-diagonal terms in the dielectric tensor are proportional to the products of two in-plane components of the moment.

4.4 Measuring spin torques with MOKE

Small changes in the moment of a magnetic material can be measured with MOKE, but it's very difficult to quantify the magnitude of the changes. However, it is possible to quantify torques with MOKE as long as a known torque can be applied and observed. One method for doing this was recently developed by Xin Fan and collaborators at the University of Delaware.[85] In this method, AC current is applied to bilayer of a magnetic material and a source of spin torque, such as a heavy metal, while an in-plane field is applied parallel to the direction of the current. PMOKE, locked in to the driving frequency of the AC current, is used to measure the magnetic response as a function of position along the strip, perpendicular to the direction of the current. In addition to any spin transfer torques on the magnetic material, the Oersted field from the current flowing in the active layer will also apply a torque to the magnetic layer. The largest component of the torque is from the in-plane component of the Oersted field, which is almost constant across the sample, while there is an out-of-plane component near the two edges of the strip. This

component, the strength of which is easily calculated, is used to determine the magnitude of the other torques on the magnetic layer. A simplified diagram of the measurement is shown in Figure 4.3.

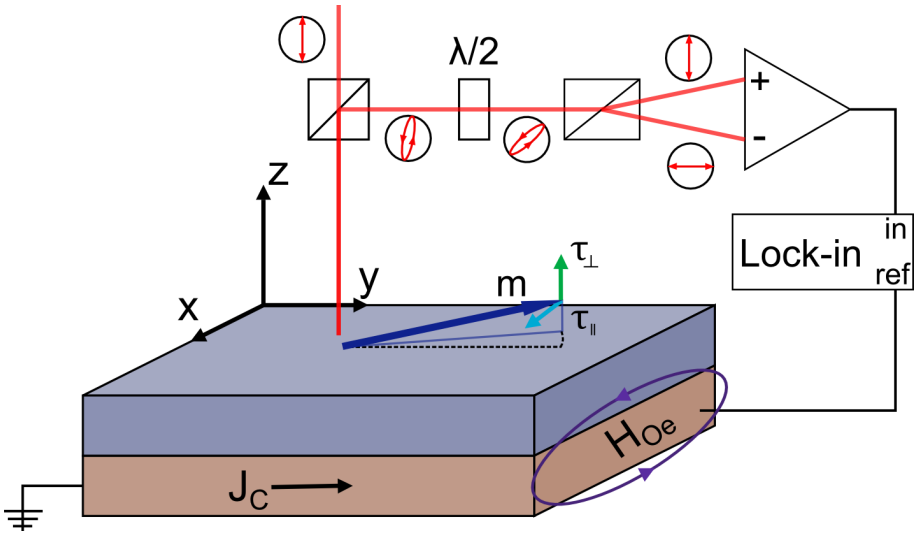

Figure 4.3. The measurement geometry used in Fan et al.,[85] *after a diagram in the same paper. An AC charge current flowing through the active layer (red) generates an Oersted field that applies torques to the magnetic layer (blue). The out-of-plane component of the Oersted field applies an in-plane torque that depends on position in the* x *direction, and is used to calibrate the measurement, which allows the determination of other torques in the* x *direction.*

The magnetic field seen at $\vec{r}$, a point along the center of the magnetic material, from a linear current density I_{active}/w at point $\vec{r}\,'$ along the center of the active material is

$$\frac{d\vec{B}}{dx'}=\frac{\mu_0 I_{active}/w}{2\pi|\vec{r}-\vec{r}\,'|}\frac{(\vec{r}-\vec{r}\,')\times\hat{y}}{|\vec{r}-\vec{r}\,'|}=\frac{\mu_0 I_{active}/w}{2\pi(t^2+(x-x')^2)}\begin{pmatrix}-t\\0\\x-x'\end{pmatrix} \qquad 4.15$$

where $t=(t_{mag}+t_{active})/2$. The field as a function of position along the strip in the magnetic material is then

$$\vec{B}(x)=\int_{-w/2}^{w/2}\frac{d\vec{B}}{dx'}dx' \tag{4.16}$$

$$B_x(x)=-\frac{I_{active}\mu_0}{2\pi w}\left(\cot^{-1}\left(\frac{2t}{w-2x}\right)+\cot^{-1}\left(\frac{2t}{w+2x}\right)\right) \tag{4.17}$$

$$B_z(x)=-\frac{I_{active}\mu_0}{4\pi w}\left(\log\left(t^2+\frac{1}{4}(w+2x)^2\right)-\log\left(t^2+\frac{1}{4}(w-2x)^2\right)\right) \tag{4.18}$$

The two components of the field are shown in Figure 4.4.

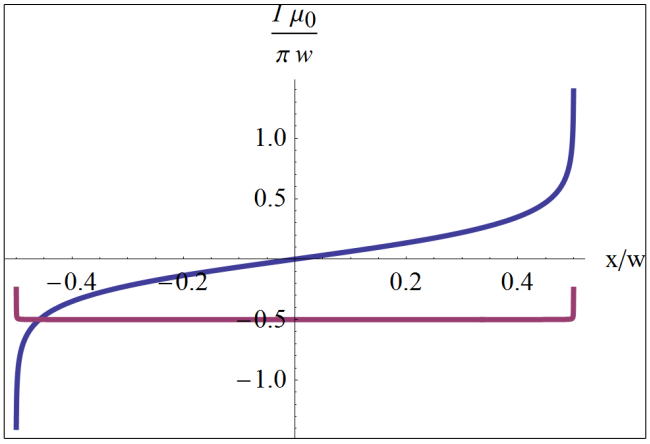

Figure 4.4. The two components of the Oersted field as a function of position along a bilayer strip. The out-of-plane field is shown in blue, the in-plane field is in purple. Here t *is 8 nm and* w *is 50 μm, typical values for our devices.*

The z component of the Oersted field has a very strong position dependence, and most importantly, the torque due to the Oersted field, $\tau_{Oe}=-\gamma\hat{m}\times\vec{B}_{Oe}$ has a different parity upon swapping the direction of the external field compared to an in-plane spin transfer torque, $\tau_{\parallel}\hat{m}\times(\hat{x}'\times\hat{m})/|\hat{x}'\times\hat{m}|$. By comparing the MOKE signal for the different directions of external fields it is possible to separate out the two components.

If the material being studied has a non-trivial quadratic MOKE effect, it can be separated out by adding a half-wave plate directly before the beam reflects off the sample. The polarization of the incident light can be rotated by the half-wave plate before reflecting off the sample, and the rotation is reversed as the beam travels back through it (except for the additional rotation and ellipticity from MOKE). By changing the angle of the half-wave plate and fitting to the component of the signal which is independent of the polarization, the PMOKE contribution can be separated from any quadratic contribution.

In addition to the AC fields created by the Oersted field (and their resulting spin torques), there will also be spin torques generated by spin currents flowing from the active layer into the magnetic layer. To first order, these should be constant across the width of the bar.

In a typical measurement, the width of the bar is ~ 50 μm and the spot size of the laser is ~ 4 μm. Both of these length scales are significantly longer that the exchange length in the materials studied (a few nm in permalloy) which allows us to locally describe the response of the magnetic material with the LLGS equation, Formula 2.1. In the steady-state case it simplifies to

$$0 = -\gamma\, \hat{m} \times \left(\vec{H}_{ext} - \hat{m} \cdot \hat{z}\, M_{eff}\, \hat{z} \right) + \tau_{\parallel} \frac{\hat{m} \times (\hat{x}' \times \hat{m})}{|\hat{x}' \times \hat{m}|} + \tau_{\perp} \frac{\hat{x}' \times \hat{m}}{|\hat{x}' \times \hat{m}|} \tag{4.19}$$

If the external field is parallel to the current direction, the out-of-plane component of the moment as a function of position x along the bar is then

$$m_z(x) = \frac{1}{\gamma} \frac{\tau_{\parallel, ST}(x) + \tau_{\parallel, Oe}(x)}{B_{ext} + \mu_0 M_{eff}} \tag{4.20}$$

Our setup, however, is incapable of measuring the moment at a single point, and instead measures over the area of the beam. Generally, the voltage signal we measure is proportional to

$$V_{signal}(x) \propto \frac{1}{P} \iint m_z(\chi) \frac{dP}{dA}(x, \chi, \psi) d\chi d\psi \qquad 4.21$$

where P is the net power of the beam, dP/dA is the intensity and χ, ψ are integration variables in the *x* and *y* directions respectively. For χ outside the width of the bar $m_z = 0$. For a symmetric Gaussian beam shape with width δ

$$V_{signal}(x) \propto \frac{1}{2\pi\delta_x\delta_y} \iint m_z(\chi) e^{-\left(\frac{(x-\chi)^2}{2\delta} + \frac{\psi^2}{2\delta}\right)} d\chi d\psi \qquad 4.22$$

The convolution of the Oersted field profiles with a Gaussian beam shape can not be expressed in a close form, but is easy to calculate numerically.

4.5 Calculating spin torques from MOKE measurements

The logistics of making such a measurement and extracting spin torques from the results is somewhat complex, and we walk through the process here. To start, we measure a lock-in voltage from our detector at positive and negative fields, V_{+B} and V_{-B}, as a function of the DC voltage applied to our fast scanning mirror V_{fsm} which is itself proportional to the position along the width of the bar, x. (The geometry of our measurement setup is described in more detail in Section 5.2). It is more instructive to work with the sum and difference of the two detector voltages

$$V_{sum} = V_{+B} + V_{-B} \quad , \quad V_{diff} = V_{+B} - V_{-B} \tag{4.23}$$

since $V_{sum}(V_{fsm})$ is only proportional to $\tau_{\parallel, Oe}(x)$ and $V_{diff}(V_{fsm})$ is only proportional to $\tau_{\parallel, ST}(x)$.

First, we fit to $V_{sum}(V_{fsm})$ to determine the relationship between the lock-in voltage and the response of the moment due to the Oersted field, $m_{z, Oe}(x)$, using

$$V_{sum}(V_{fsm}) = \frac{dV_{lockin}}{dm_z} \cdot \frac{I_{net}\mu_0}{2\pi w(B_{ext} + \mu_0 M_{eff})} \cdot \left(\log\left(t^2 + \frac{1}{4}\left(w + 2\frac{dx}{dV_{fsm}}(V_{fsm} - V_c)\right)^2\right) - \log\left(t^2 + \frac{1}{4}\left(w - 2\frac{dx}{dV_{fsm}}(V_{fsm} - V_c)\right)^2\right)\right) * G(x, \delta) \tag{4.24}$$

where $*G(x, \delta)$ represents a convolution with a Gaussian beam profile of width δ as described above. We fit to four parameters, dV_{lockin}/dm_x which relates the lock-in signal to the response of the magnet, V_c the mirror voltage that corresponds to the center of the bar, dx/dV_{fsm} the scaling factor that relates mirror voltage to actual position, and δ. Note that a factor of two has been added to account for the fact that the effect of the Oersted field appears twice in $V_{sum}(V_{fsm})$.

Next, we fit $V_{diff}(V_{fsm})$ to

$$V_{diff}(V_{fsm}) = G(x,\delta) * \frac{dV_{lockin}}{dm_z} \frac{2\tau_{\parallel,ST}}{\gamma(B_{ext}+\mu_0 M_{eff})} \begin{cases} 1 & , \left|V_{fsm}-V_c\right| \frac{dx}{dV_{fsm}} \leq \frac{w}{2} \\ 0 & , \left|V_{fsm}-V_c\right| \frac{dx}{dV_{fsm}} > \frac{w}{2} \end{cases} \quad 4.25$$

keeping constant the values of dx/dV_{fsm}, dV_{lockin}/dm_x, V_c and δ as determined from the first fit, and fitting to the value of $\tau_{\parallel,ST}$. Again, there is a factor of two from the definition of $V_{diff}(V_{fsm})$. From this, we can calculate the spin torque conductivity using Formula 2.23

$$\sigma_{\parallel} = \tau_{\parallel,ST} \frac{2e}{\hbar} \frac{M_s t_{mag} w}{I_{net} R_{sq} \gamma} \quad 4.26$$

There is also an alternate method for calculating the spin torque conductivity, which makes the calculation easier and avoids the use of parameters which don't appear in the final calculation. The first step is to note that since $t_{mag} \ll w$ we can approximate $V_{sum}(V_{fsm})$ as

$$V_{sum}(V_{fsm}) = \frac{dV_{lockin}}{dm_z} \cdot \frac{I_{net}\mu_0}{2\pi w(B_{ext}+\mu_0 M_{eff})} \cdot \left(\ln\left(\frac{1}{4}\left(w+2\frac{dx}{dV_{fsm}}(V_{fsm}-V_c)\right)^2\right) - \ln\left(\frac{1}{4}\left(w-2\frac{dx}{dV_{fsm}}(V_{fsm}-V_c)\right)^2\right)\right) * G(x,\delta) \quad 4.27$$

We can then use the fact that

$$\int_{V_c}^{V_c + w/(2\,dx/dV_{fsm})} \left(\ln\left(\frac{1}{4}\left(w + 2\frac{dx}{d\,V_{fsm}}(V_{fsm} - V_c) \right)^2 \right) - \ln\left(\frac{1}{4}\left(w - 2\frac{dx}{d\,V_{fsm}}(V_{fsm} - V_c) \right)^2 \right) \right) dV_{fsm} = \frac{w \ln(4)}{dx/dV_{fsm}} \quad 4.28$$

to show that the total area under the curve is

$$A_{sum} = \int_{-\infty}^{\infty} \left| V_{sum}(V_{fsm}) \right| dV_{fsm} = \frac{dV_{lockin}}{dm_z} \frac{I_{net}\mu_0}{\pi(B_{ext} + \mu_0 M_{eff})} \frac{\ln(4)}{dx/dV_{fsm}} \quad 4.29$$

It is possible to estimate the area under these curves, and the exact area is easily calculated by fitting to the exact functions above or summing over the experimental data. For example, Figure 4.5 shows data for a representative device as well as fits to Formulas 4.25 and 4.27.

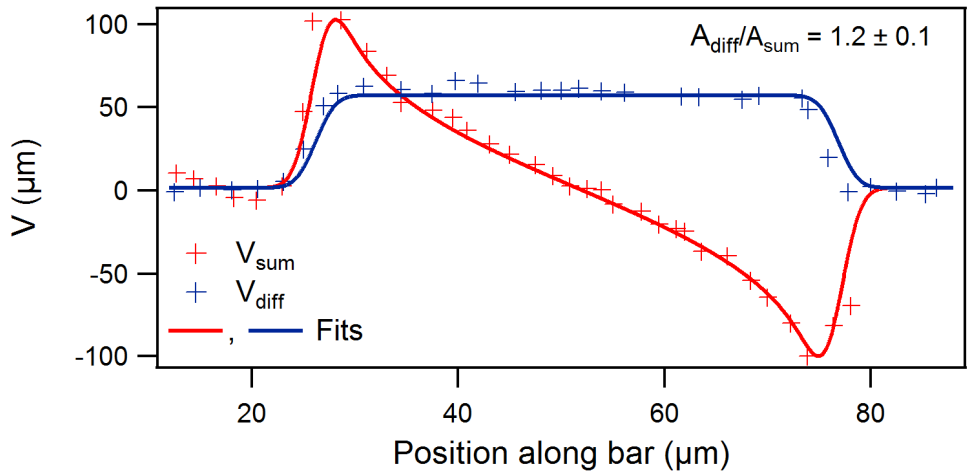

Figure 4.5. Line scan data for a device with 6 nm of platinum and 8 nanometers of permalloy taken at Delaware. After fitting to the two voltage signals, the ratio of the areas traced out by both curves can be easily calculated, and is 1.2 ± 0.1 in this case.

The area under the curve for $V_{diff}(V_{fsm})$ as defined in Formula 4.25 is just

$$A_{diff} = \int_{-\infty}^{\infty} \left| V_{diff}(V_{fsm}) \right| dV_{fsm} = \frac{dV_{lockin}}{dm_z} \frac{2\tau_{\parallel, ST}}{\gamma(B_{ext} + \mu_0 M_{eff})} \frac{w}{dx/dV_{fsm}} \tag{4.30}$$

The ratios of these two areas then has the simple expression

$$\frac{A_{diff}}{A_{sum}} = \frac{2\pi\tau_{\parallel, ST} w}{\gamma I_{net} \mu_0 \ln(4)} \tag{4.31}$$

and solving for the torque we have

$$\tau_{\parallel, ST} = \frac{A_{diff}}{A_{sum}} \frac{\gamma I_{net} \mu_0 \ln(4)}{2\pi w} \tag{4.32}$$

Plugging this into Formula 4.26 we have

$$\sigma_{\parallel} = \frac{A_{diff}}{A_{sum}} \frac{2e}{\hbar} \frac{\mu_0 M_s t_{mag} \ln(4)}{2\pi R_{sq}} \tag{4.33}$$

This is a useful expression since it depends only on a few parameters. In particular, we don't even need to know the current that was flowing through the device or the width of the bar. The spin torque ratio is similarly

$$\theta_{\parallel} = \frac{A_{diff}}{A_{sum}} \frac{2e}{\hbar} \frac{\mu_0 M_s t_{mag} \ln(4)}{2\pi R_{sq} \sigma_{active}} \tag{4.34}$$

This formula allows for easy estimation of the spin torque ratio, since both A_{diff}/A_{sum} and $(2e/\hbar)\mu_0 M_s t_{mag} \ln(4)/2\pi R_{sq}\sigma_{active}$ are unitless. For the device shown in Figure 4.5,

$(2e/\hbar)\mu_0 M_s t_{mag} \ln(4)/2\pi R_{sq} \sigma_{active} \approx 0.067$ and $A_{diff}/A_{sum} = 1.2 \pm 0.1$, which implies that $\theta_{\parallel} = 0.08 \pm 0.1$.

5. MOKE Measurements of Spin Torques in Platinum and Bismuth Selenide

In Chapter 4 we discussed how it is possible to measure in-plane spin torques optically. This is a very new method, and at the time of writing, results on materials with non-negligible MLD are still in preparation. In order to make certain that this method works, the obvious first step is to perform both electric and optical measurements of spin torques in the same system and make sure that they agree. In this chapter we compare both classes of measurements on platinum/permalloy bilayers and present initial data on bismuth selenide/permalloy bilayers, similar to those studied in Chapter 3. In each case, several types of devices were fabricated simultaneously on the same die so that all measurements can be performed on identical bilayers.

We discuss the growth and fabrication of both types of films, and the experimental setups used for MOKE measurements at both Cornell and Delaware. We present full sets of data taken using the MOKE setup at Delaware, as well as data taken on the recently-completed setup at Cornell, which will eventually allow low-temperature measurements. We compare these to electrical measurements made on the same films using different electric measurement techniques, and discuss possible reasons for differences between the techniques.

5.1 Sample growth and characterization

The platinum/permalloy bilayers were grown in “The Lesker”, a six gun magnetron sputtering system housed in CCMR and managed by members of the Ralph group. In each bilayer 6 nm of platinum was deposited on clean epi-ready sapphire substrates without a wetting layer at a power of 25 W and a pressure of 3.5 mTorr, followed by the desired thickness of permalloy at 50 W and 2.5 mTorr. Each film was capped with 2 nm of metallic aluminum, which was oxidized with a

dry nitrogen/oxygen mixture before being removed from the chamber.

The saturation magnetization of the permalloy films was measured using the vibrating sample magnetometer mode of CCMR's Physical Property Measurement system, and the data is shown in Figure 5.1.

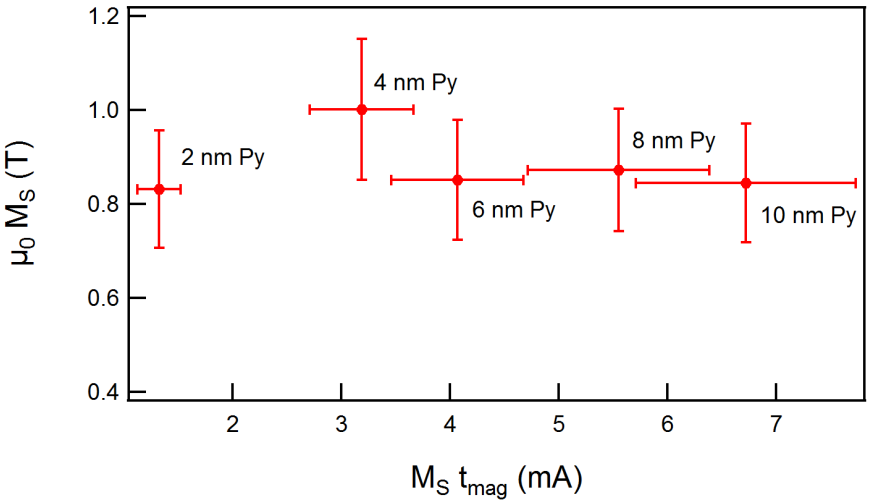

Figure 5.1. VSM measurements for the platinum/permalloy layers. The saturation magnetization, shown on the vertical axis, is largely constant as expected, and the magnetization-thickness product, shown on the horizontal axis, scales roughly linearly with thickness as expected.

The sheet resistances of the platinum/permalloy bilayers are summarized in Table 5.1.

Py thickness (nm)	$R_{\square}(\Omega)$
0	51.7
2	38.0
4	29.4
6	24.6
8	21.7
10	17.3

5.1

The bismuth selenide thin films were grown by the Samarth group at Penn State using the

methods described in Reference 64, and the samples were processed into bilayer films with permalloy as described in Section 3.2. The saturation magnetization of these films is summarized in Figure 5.2.

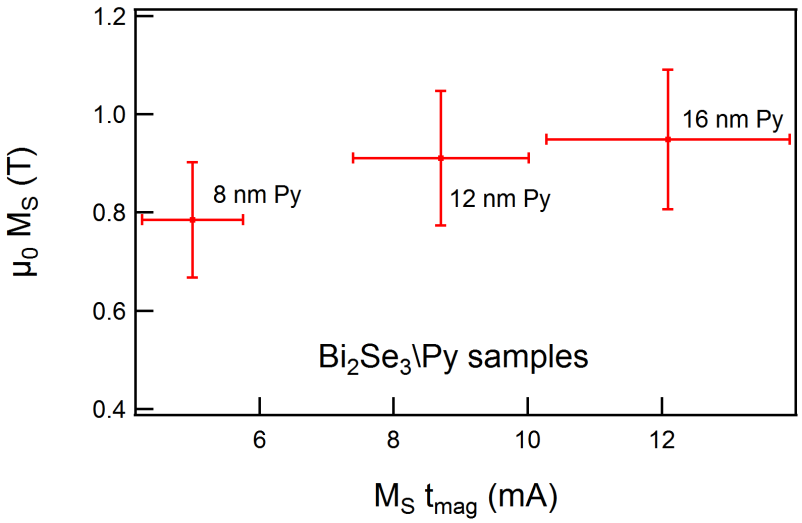

Figure 5.2. VSM measurements for the bismuth selenide/permalloy layers.

The sheet resistances of the bismuth selenide/permalloy bilayers are summarized in Table 5.2.

Py thickness (nm)	$R_{\square}(\Omega)$
0	1408.2
8	62.4
12	36.7
16	26.0

5.2

The AMR of each ST-FMR device was characterized using the same technique described in Section 3.2.

5.2 Experimental setup for optical measurements

Our scanning PMOKE system is shown schematically in Figure 5.3.

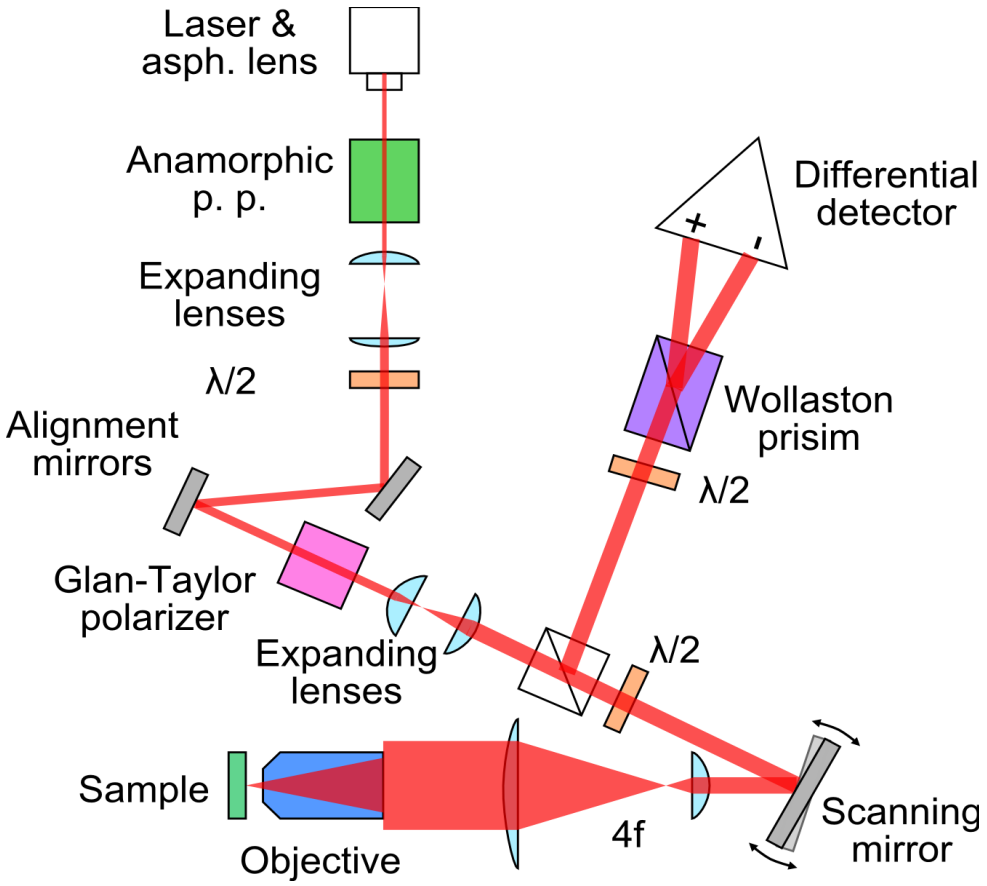

Figure 5.3. Schematic diagram of the optics for the MOKE setup at Cornell, not to scale. The half-wave plate between the two four-f lens systems is mounted on a computer-controlled rotation stage. The sample is located between the poles of a water-cooled barrel type magnet which can apply up to 0.7 T in-plane. The Delaware setup, and older version of which is shown in detail in Reference [85], is significantly simpler because it uses stage scanning.

Our 658 nm wavelength laser is mounted on a temperature-controlled stage. An aspherical lens collimates the diverging beam from the laser diode, and an anamorphic prism pair corrects for the ellipticity of the beam, resulting in a ~ 3 mm diameter, roughly circular beam, and a pair of plano-concave lenses expands this to ~ 5 mm. A pair of alignment mirrors on mirror mounts allows us to align the optics before and after the mirror pair independently.

The beam emerging from the diode is partially polarized parallel to the surface of the optical table, and a half-waveplate rotates this polarization 90º so that less power is lost when passing

the beam through a Glan-Taylor polarizer, which polarizes the beam perpendicular to the surface of the table (s-polarized). After the polarizer a second lens pair further expands the beam up to a ~9 mm diameter, and a 1" half-wave plate on a computer controlled rotation stage allows us to rotate the polarization to different angles.

We use a 1" fast scanning mirror from Optics in Motion for scanning in our system. This has several advantages over mechanical stage scanning as it removed the need for moving parts (which often have magnetic components) near the magnet, and allows for easy switching between a room-temperature sample stage and an optical cryostat. Its primary drawback is that it requires significantly more complex optics, and can distort the otherwise well-controlled polarization state of our beam.

The fast steering mirror allows us to send the beam off at a range of angles from the point at which the incoming beam strikes the surface of the mirror. However, if we would like to focus the beam with a microscope objective, what we really need is for the beam to hit a stationary point (the back of the microscope objective) incident from a range of directions. A four-f lens system, also known as a confocal lens pair, makes this possible.[86] In such a system, the scanning mirror is placed the focal length away from a lens. A second lens is placed its focal length plus the focal length of the first lens away from the first lens. As long as the collimated bean from the mirror reaches the first lens, it will always pass through a fixed point one focal length beyond the second lens, as shown in detail in Figure 5.4.

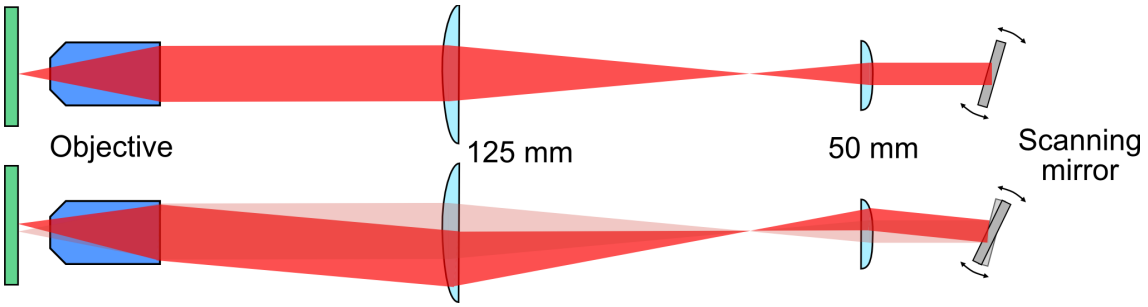

Figure 5.4. Diagram of the sample branch of our optical path, with focal lengths for a typical setup shown. Distances and the height of elements are approximately to scale, although the complex optical path inside the objective has been simplified and the beam width has been slightly reduced for clarity. In the top frame, the mirror directs the beam directly through the center of all lens elements. In the lower frame the mirror directs the beam slightly off the center of the first lens, although the beam always strikes the center of the back of the objective.

When the optics in our system are well-aligned, it is possible to resolve features down to a few μm. Figure 5.5 shows an image of a Hall bar device taken with the setup at Cornell.

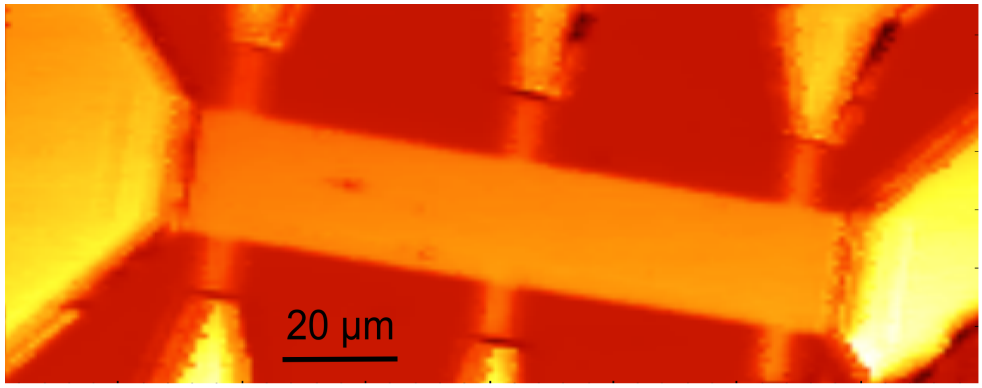

Figure 5.5. Sample image taken with the MOKE setup at Cornell. The color corresponds to the DC reflectivity, and the spot size is ~ 2 μm. The design width of the small voltage leads on the side of the main bar is 5 μm.

5.3 Sample MOKE measurements at Cornell

Using the MOKE setup at Cornell, we characterized some of our our platinum/permalloy samples. When the beam is either s- or p-polarized at the sample, these devices show a pronounced quadratic MOKE effect, as shown in Figure 5.6.

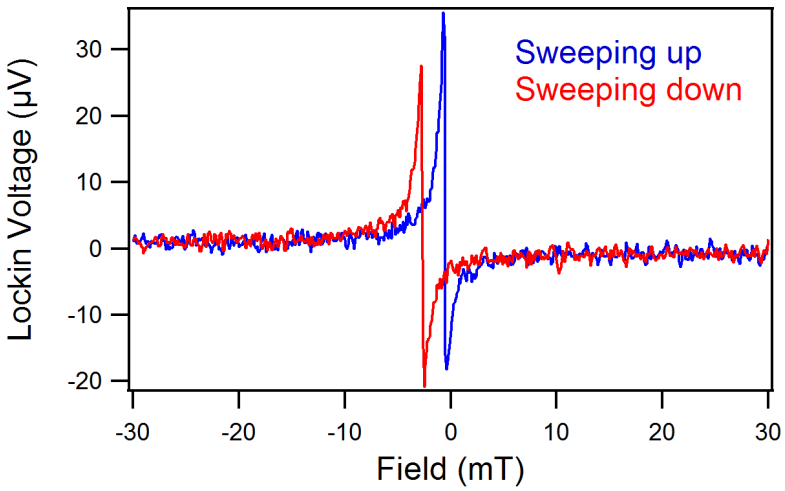

Figure 5.6. Voltage from our split photodetector, locked in to the driving current flowing through a 6 nm Pt / 8 nm Py device. The laser is directed at the center of a 50 μm bar, and the driving current is ~ 8 mA. The polarization at the device is s-polarized, perpendicular to both the plane of the optical table and the current direction.

The quadratic MOKE effect appears as the pronounced peaks near zero field, which fall off quickly with field. A very small linear MOKE effect can also be seen as the slight difference between positive and negative field, largely independent of field as per Formula 4.20. For p-polarized beams, a similar magnetic field sweep would look identical to Figure 5.6 except for a reflection across the vertical axis, as expected per Formula 4.13 and 4.14.

When the final half-wave plate is set to 22.5°, the beam at the sample is polarized at 45°, an even mixture of s- and p-polarizations. At this angle, the larger quadratic MOKE response vanishes leaving only the linear MOKE signal. A representative magnetic field sweep is shown in Figure 5.7.

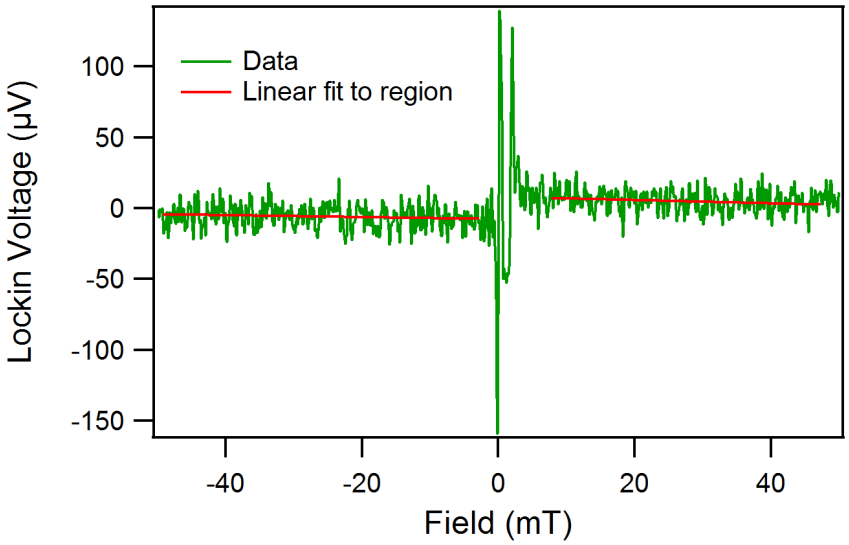

Figure 5.7. Voltage from our split photodetector, locked in to the driving current flowing through the same 6 nm Pt / 8 nm Py device shown in in Figure 5.6. The laser is directed at the center of a 50 μm bar, and the driving current is ~ 8 mA. The polarization at the device is 45°, evenly mixed between s- and p-polarization to separate out the linear MOKE component. Near zero field the moment is no longer saturated and the signal oscillates randomly.

Now that we have removed the quadratic MOKE signal, we can take a line scan measurement of the type discussed in Section 4.4.

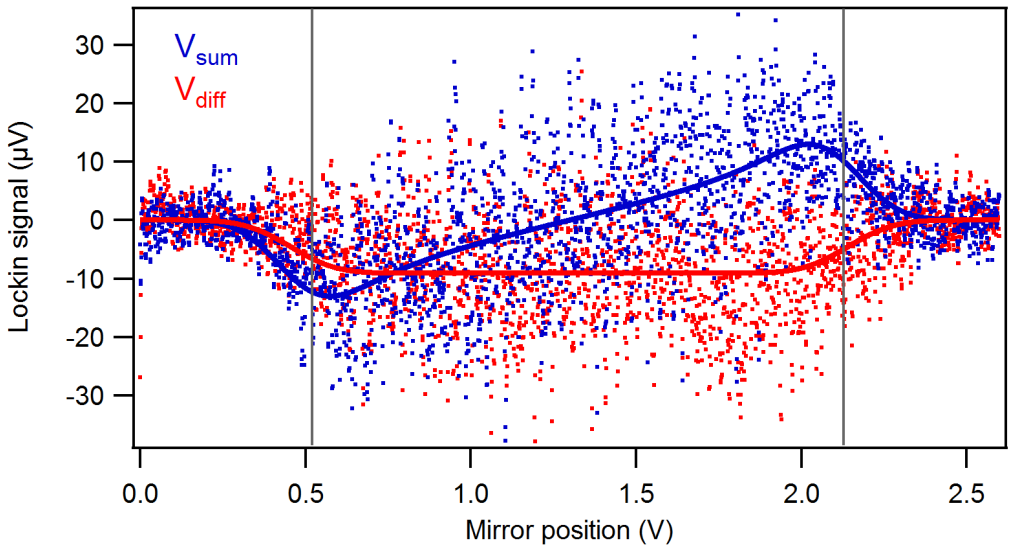

Figure 5.8. Line scan measurement of the same device as in Figure 5.6 using the same drive current with an applied field of 30 mT. Data is shown as scattered points due to the large noise,

and fits to Formulas 4.25 and 4.27 are shown as solid lines.

This measurement is quite noisy, as can be expected from the fact that the linear offset in the saturated regions in Figure 5.7 is smaller than the RMS noise. Nevertheless, the expected signals are clearly visible. From this measurement it appears that the beam width is on the order of ~ 10 μm, which is somewhat larger than expected from our DC images taken with the fast scanning mirror.

First, we fit V_{sum} to Formula 4.2 and find that $dV_{lockin}/dm_x = -0.076 \pm 0.003$ V, $V_{center} = 1.300 \pm 0.003$ V, $dx/V_{fsm} = 29.5 \pm 0.02$ μm/V, and $\delta = (88 \pm 8) \times \Delta V_{fsm}$ where ΔV_{fsm} is the fast scanning mirror step length along the line, 0.01 V here. We then reuse all these values to fit to V_{diff}, although only dV_{lockin}/dm_x is directly related to the measured torque. The ratio of areas is $A_{diff}/A_{sum} = 1.2 \pm 0.1$ and we find that $\tau_{\parallel,ST} = (5.3 \pm 0.1) \times 10^{-5}$ T in field units and $\sigma_{\parallel} = (2.5 \pm 0.4) \times 10^{5}$ $\hbar/2e\ \Omega^{-1} m^{-1}$. Dividing by $\sigma_{active} \approx 3.23 \times 10^{6}$ $\Omega^{-1} m^{-1}$ this suggests that $\theta_{\parallel} = 0.08 \pm 0.01$, which agrees well with previous measurements and those presented below in Section 5.4.

5.4 MOKE and electrical measurements of spin torques in platinum and bismuth selenide

While we have made initial measurements using the Cornell setup, the signal-to-noise ratio with out mirror-based setup is lower than the setup at Delaware. Because of this, we present MOKE data here taken by our collaborators at Delaware. In addition to the MOKE-based measurements, we also performed several types of electrical measurements for the spin torque efficiencies in the same set of samples. These include ST-FMR measurements of the type discussed in Section 3.2, DC-mixing measurements of the type discussed in Section 2.8, and 2nd

harmonic planar Hall effect measurements performed at Delaware by Xin Fan and Tao Wang as described in References [85] and [87].

In the platinum/permalloy samples it is much easier to calculation the portion of the current that flows through the platinum layer since the resistivity of permalloy is much closer to that of platinum than it is to that of bismuth selenide. Because of this, we present our results in terms of the spin torque efficiencies, as in Section 3.4. A summary of the in-plane spin torque efficiencies is shown in Figure 5.9.

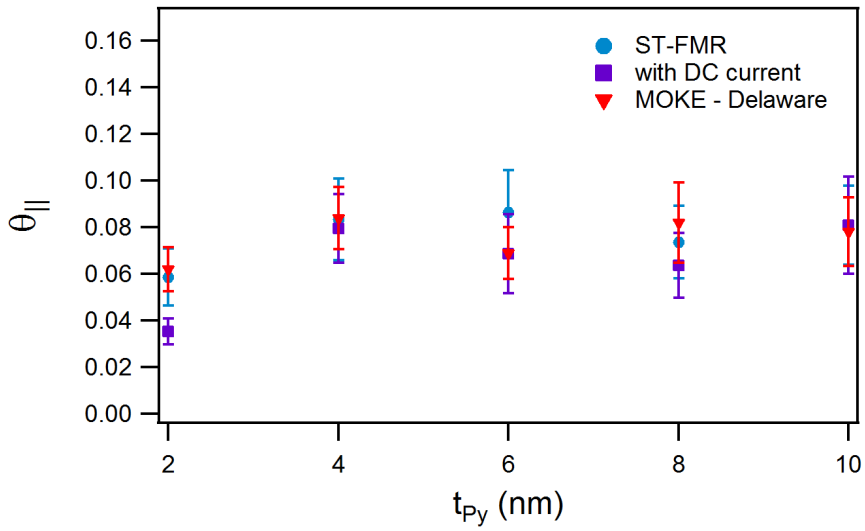

Figure 5.9. The effective in-plane spin torque ratio for the platinum/permalloy layers, measured by multiple techniques. With the exception of the sample with the thinnest permalloy layer, all the measurements agree to within the experimental uncertainty (which suggests we may slightly overestimate the error in these measurements.

For permalloy thicknesses above 2 nm the spin torque ratio is largely constant. At 2 nm the spin torque ratio is roughly half its value at larger thicknesses. With the exception of the 2 nm sample, all three methods agree to within one standard error.

The out-of-plane spin torque efficiencies, including the MOKE measurements done at Delaware

are shown in Figure 5.10.

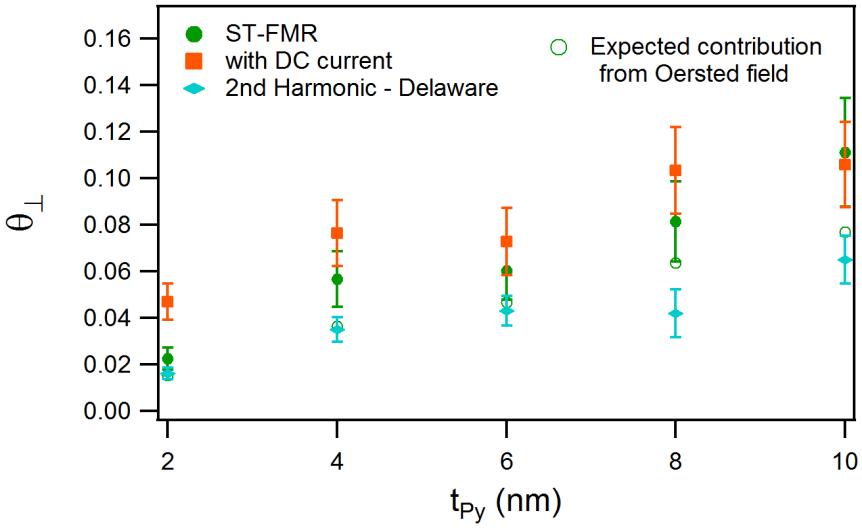

Figure 5.10. The out-of-plane spin torque ratio for the platinum/permalloy layers, measured by multiple techniques as well as the expected contribution from the Oersted field generated by the current flowing in the platinum layer.

The ST-FMR measurements agree with the DC-mixing measurements to within the experimental uncertainty (except for the thinnest permalloy thickness), and both are roughly 50% larger than the expected contribution from the Oersted field. The 2nd harmonic measurements made at Delaware are closer to the expected contribution from the Oersted field, and are clearly lower on average than the other two measurements.

We also made the same set of measurements on the bismuth selenide/permalloy devices. While these devices were straightforward to measure with ST-FMR, we saw significant changes in both the resonant field and damping that were *even* in DC current. This is presumably due to heating, and was significantly stronger than was seen in the devices discussed in Chapter 3. A typical measurement is shown in Figure 5.11.

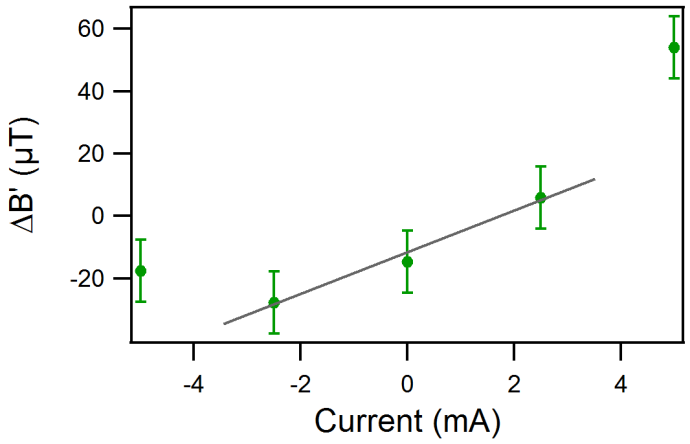

Figure 5.11. Change in apparent field as a function of applied DC current for an 80 μm × 16 μm device with 8 nm of bismuth selenide and 8 nm of permalloy. Each data point represents an average shift over frequencies between 6 and 10 GHz. While the shift is approximately linear at low applied currents (gray line added to guide the eye) at higher currents there is a clear non-linear contribution.

This component, roughly quadratic in applied current, can not be easily eliminated as measuring at smaller DC currents also reduces the signal-to-noise ratio of the measurement. Because of this, we were unable to obtain statistically significant measurements using this method on these devices.

We also present the results of measurements on the bismuth selenide/permalloy layers in terms of the effective spin torque ratios for easy comparison to the platinum/permalloy results. This assumes an active layer conductivity of $\sigma_{active} \approx 8.9 \times 10^4 \ \ \Omega^{-1} m^{-1}$, and this is subject to the same considerations discussed in Section 3.4. The effective in-plane spin torque ratios measured for the bismuth selenide/permalloy samples are shown in Figure 5.12.

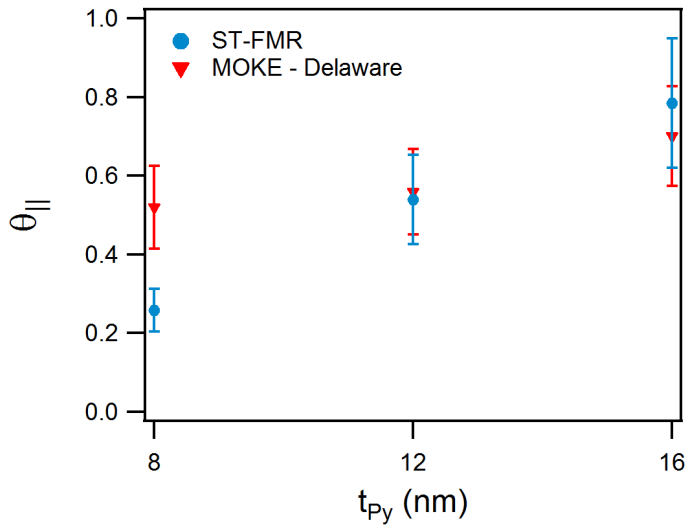

Figure 5.12. The effective in-plane spin torque ratio for the bismuth selenide/permalloy layers, measured by ST-FMR and MOKE. With the exception of the sample with the thinnest permalloy layer, all the measurements agree to within the experimental uncertainty.

There is a noticeable upward trend in the spin torque ratio measured by ST-FMR which is not significantly seen in the MOKE measurements. A similar trend was also seen in the ST-FMR measurements described in Chapter 3. The overall values are also similar to the comparable samples from Chapter 3, although there is a larger proportional increase in the spin torque ratio between the devices with 8 nanometers and 16 nanometers of permalloy.

The effective out-of-plane spin torque ratios measured for the bismuth selenide/permalloy samples are shown in Figure 5.13.

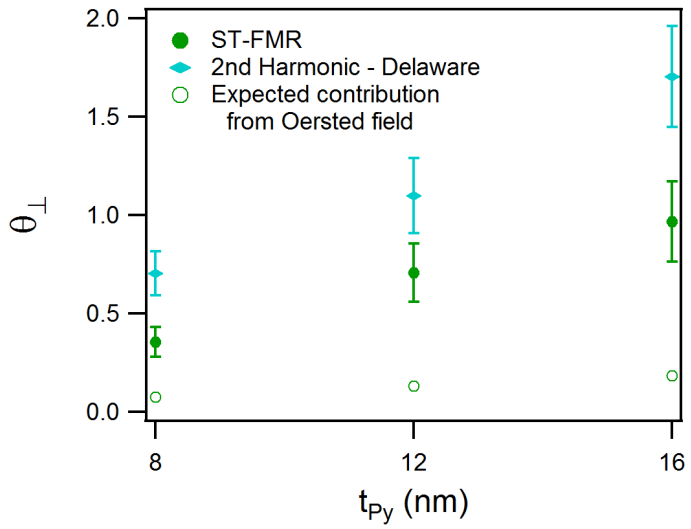

Figure 5.13. The effective out-of-plane spin torque ratio for the bismuth selenide/permalloy layers, measured by ST-FMR and the 2nd harmonic method. None of the measurements agree to within the experimental uncertainty, with the 2nd harmonic measurements nearly twice as large on average.

The out-of-plane spin torque ratios measured by the 2nd harmonic method are significantly larger than those measured by ST-FMR, although both show a clear trend of increasing with increasing permalloy thickness. This is in contrast to the measurements on platinum, where the 2nd harmonic method reported a smaller spin torque ratio than ST-FMR. The values of the out-of-plane spin torque ratios measured by ST-FMR are comparable to those made on similar devices in Chapter 3, and again all measurements find values significantly larger than would be expected from the Oersted field alone.

5.5 Discussion and ongoing work

In Section 5.4 we saw that the MOKE measurements of the in-plane spin torque agree well with the two types of ST-FMR measurement in platinum, which suggests that this type of MOKE measurement will allow accurate measurements of spin torques in systems with magnetic insulators or that are otherwise not amendable to ST-FMR measurements. This general agreement between the two methods was also observed in measurements of the in-plane spin

torque in bismuth selenide, which suggests that it is also a practical method where relatively little of the applied current flows through the active layer. By contrast, measurements of the out-of-plane spin torques by the 2nd harmonic method and ST-FMR did not agree nearly as well. In platinum/permalloy samples the values measured by the 2nd harmonic method were consistently at least 1 standard error below those measured by ST-FMR. In the bismuth selenide/permalloy devices, however, this disagreement was reversed and the 2nd harmonic method reported values more than 1 standard error larger than those measured by ST-FMR. This suggests that additional care needs to be taken to avoid heating and other possible artifacts with these types of measurements. Determining the source of these discrepancies and reducing the uncertainty in the various measurements is an active area of research.

In this chapter we saw that MOKE measurements of in-plane spin torques agree well with ST-FMR measurements in systems with metallic ferromagnetic layers. This suggests that optical measurements of spin torques are excellent candidates for systems with insulating ferromagnetic layers. In order to confirm this, we are preparing to measure devices with room-temperature insulating ferromagnetic layers like yttrium-iron-garnet, and then to move on to more exotic magnetic layers like magnetically-doped topological insulators which will require the use of an optical cryostat.

6. Appendices

6.1 Recipes and protocols related to nanofabrication

Standard photolithography process using the 5× stepper at CNF

This is the recipe that we normally use for both etch and liftoff steps. It can reliably produce features as small as 1 μm. For long etches it it may be best to replace the S-1805 with a thicker formulation like S-1813.

1. Spin LOR-3A in the class 2 room for 60 s at 3000 RPM with 1000 RPM/s acceleration.
2. Bake 5 min at 180 C.
3. Spin S-1813 for 60 s at 3000 RPM with 1000 RPM/s acceleration.
4. Bake 1:15 at 115 C for sapphire substrates.
5. Expose 0.26 seconds in the 5x stepper.
6. Develop for 1:30 in 726-MIF developer using minimal agitation.
7. Rinse in DI water.

For liftoff processes, soaking overnight in room temperature 1165 followed by ~5 sec of sonication is normally sufficient. For etch processes, soaking 1-2 hours in 180 C 1165 is recommended, a process that was refined by Jen Grab.

Mounting small pieces in the 5× stepper

Pieces which can fit entirely inside the smallest ring on the 3" stage are easy to deal with – simply use the ring-shaped wafer to block the other vacuum rings. Samples which are larger

than this pose a bit of a problem. After some trial and error, we think that the best method is to take a sheet of cleanroom safe paper, preferably the blue printer kind. Carefully cut out the shape of a 3” wafer without wrinkling the paper. Next, use a razor to carefully cut out a central region which will fit entirely inside your smallest sample that you need to mount. Use this underneath the sample. Make sure that you can still focus on the surface of the sample, if it's outside the focusing range you may need to use a different height stage. The blue latex-infused printer paper is recommended because it's thinner than most other cleanroom-safe papers, and will add less height to the sample. It's also very airtight.

Removing selenium caps from MBE-grown bismuth selenide in the Lesker sputtering system

Take a sheet of thick aluminum foil and cut it into a circle slightly smaller than the copper backing plate for the disk. Take the stainless steel front plate for a disk with a 2×2 inch holder for double-size glass slides. Stick one of the 1×2 inch glass slide pieces in the holder so that there's still a 1×2 inch open area. Cut out holes which are slightly smaller than the samples you want to remove in the center of the aluminum foil. If there are too many for the space, remove the piece of the glass slide. Flatten the foil by putting it between pages in the dictionary that is stored on top of the sample cabinet and press hard on both covers. Lay the foil across the opening in the stainless sample holder, and carefully place the samples face-down in the holes. Place the copper backing plate behind the samples to clamp them against the taught tinfoil. Load the disk carefully into the Lesker to make sure that none of the samples will come loose. This mounting avoids the need to use cured silver paint or similar, but is not recommended for higher temperatures.

After transferring the disk into the main chamber, heat to 240 C over 30 minutes with the sample shutter closed. Stay with the heater for the first few minutes to make sure the sample is properly warming up. Keep at 240 C for an hour, then turn off the heat. Allow at least 4 hours to cool before depositing subsequent layers.

6.2 Simultaneous fits for ST-FMR measurements with applied DC currents

When we make ST-FMR measurements with DC current (as described in Section 2.8), we produce a lot of data. Normally we measure between 6 and 10 GHz and 1 GHz intervals, and over at least five values of applied DC current, for a minimum of 25 resonance peaks. If we were to fit to each resonance peak individually, we would need to determine a value for M_{eff}, α, $\tau_{\perp,RF}$, $\tau_{\parallel,RF}$, $\tau_{\perp,DC}$, and $\tau_{\parallel,DC}$ at each peak, which would give us at least 150 degrees of freedom in the fits. Fortunately, we can reduce this by taking into account the fact that many of these parameters should be independent of the DC current, frequency, or both. In particular, the damping parameter α should be common between all resonances, $\tau_{\perp,DC}$ and $\tau_{\parallel,DC}$ should depend only on the DC current, and M_{eff}, $\tau_{\perp,RF}$ and $\tau_{\parallel,RF}$ should depend only on the frequency. M_{eff} is close to constant in many devices, but can have a slight frequency dependence in some devices.

In order to take advantage of this reduction in the number of degrees of freedom, we need to fit all resonances in the set simultaneously. This complicates the fitting process somewhat, but is easy to accomplish with analysis software like IgorPro. Sample code for this process can be found on the Ralph Group GitHub (https://github.com/ralph-group/Shared-Igor-analysis-routines).

7. References

1. Null, L., Null, P. S. U. L. & Lobur, J. *The Essentials of Computer Organization and Architecture*. (Jones & Bartlett Publishers, 2014).
2. Staff, bit-tech. Intel Sandy Bridge Review. *bit-tech* at <http://www.bit-tech.net/hardware/cpus/2011/01/03/intel-sandy-bridge-review/1>
3. Why SSDs Are Awesome: An SSD Primer | Samsung SSD. at <http://www.samsung.com/global/business/semiconductor/minisite/SSD/global/html/about/whitepaper01.html>
4. Samsung SSD 840: Testing the Endurance of TLC NAND. at <http://www.anandtech.com/show/6459/samsung-ssd-840-testing-the-endurance-of-tlc-nand>
5. Wuttig, M. Phase-change materials: Towards a universal memory? *Nat. Mater.* **4,** 265–266 (2005).
6. Lankhorst, M. H. R., Ketelaars, B. W. S. M. M. & Wolters, R. A. M. Low-cost and nanoscale non-volatile memory concept for future silicon chips. *Nat. Mater.* **4,** 347–352 (2005).
7. Wong, H.-S. P. *et al.* Metal-Oxide RRAM. *Proc. IEEE* **100,** 1951–1970 (2012).
8. Hayashi, M., Thomas, L., Moriya, R., Rettner, C. & Parkin, S. S. P. Current-Controlled Magnetic Domain-Wall Nanowire Shift Register. *Science* **320,** 209–211 (2008).
9. Racetrack Is Making Slow but Sure Progress | EE Times. *EETimes* at <http://www.eetimes.com/document.asp?doc_id=1324269>
10. Kawahara, T., Ito, K., Takemura, R. & Ohno, H. Spin-transfer torque RAM technology: Review and prospect. *Microelectron. Reliab.* **52,** 613–627 (2012).
11. Akerman, J. APPLIED PHYSICS: Toward a Universal Memory. *Science* **308,** 508–510 (2005).
12. Chappert, C., Fert, A. & Van Dau, F. N. The emergence of spin electronics in data storage. *Nat. Mater.* **6,** 813–823 (2007).
13. Tehrani, S. *et al.* Progress and outlook for MRAM technology. *IEEE Trans. Magn.* **35,** 2814–2819 (1999).
14. Park, W., Song, I.-H., Park, S. & Kim, T. Technology of MRAM (Magneto-resistive Random Acces Memory) Using MTJ(Magnetic Tunnel Junction) Cell. *J. Semicond. Technol. Sci.* **2,** (2002).
15. Slonczewski, J. C. Conductance and exchange coupling of two ferromagnets separated by a tunneling barrier. *Phys. Rev. B* **39,** 6995–7002 (1989).
16. Ralph, D. C. & Stiles, M. D. Spin transfer torques. *J. Magn. Magn. Mater.* **320,** 1190–1216 (2008).

17. Slonczewski, J. C. Current-driven excitation of magnetic multilayers. *J. Magn. Magn. Mater.* **159,** L1–L7 (1996).

18. Berger, L. Emission of spin waves by a magnetic multilayer traversed by a current. *Phys. Rev. B* **54,** 9353–9358 (1996).

19. Katine, J., Albert, F., Buhrman, R., Myers, E. & Ralph, D. Current-Driven Magnetization Reversal and Spin-Wave Excitations in Co /Cu /Co Pillars. *Phys. Rev. Lett.* **84,** 3149–3152 (2000).

20. Huai, Y., Albert, F., Nguyen, P., Pakala, M. & Valet, T. Observation of spin-transfer switching in deep submicron-sized and low-resistance magnetic tunnel junctions. *Appl. Phys. Lett.* **84,** 3118–3120 (2004).

21. Fuchs, G. D. *et al.* Spin-transfer effects in nanoscale magnetic tunnel junctions. *Appl. Phys. Lett.* **85,** 1205–1207 (2004).

22. Everspin ships first ST-MRAM memory with 500X performance of flash. *Computerworld* (2012). at <http://www.computerworld.com/article/2493603/data-center/everspin-ships-first-st-mram-memory-with-500x-performance-of-flash.html>

23. 29, J. H. on O. & Pm, 2014 at 4:32. Everspin teams up with GlobalFoundries to build commercial MRAM. *ExtremeTech* at <http://www.extremetech.com/computing/193065-mram-manufacturer-everspin-teams-up-with-globalfoundries-to-build-magnetic-memory>

24. D'Yakonov, M. I. & Perel', V. I. Possibility of Orienting Electron Spins with Current. *ZhETF Pisma Redaktsiiu* **13,** 657 (1971).

25. Hirsch, J. E. Spin Hall Effect. *Phys. Rev. Lett.* **83,** 1834–1837 (1999).

26. Kato, Y. K., Myers, R. C., Gossard, A. C. & Awschalom, D. D. Observation of the Spin Hall Effect in Semiconductors. *Science* **306,** 1910–1913 (2004).

27. Valenzuela, S. O. & Tinkham, M. Direct electronic measurement of the spin Hall effect. *Nature* **442,** 176–179 (2006).

28. Liu, L., Buhrman, R. A. & Ralph, D. C. Review and Analysis of Measurements of the Spin Hall Effect in Platinum. *ArXiv11113702 Cond-Mat* (2011). at <http://arxiv.org/abs/1111.3702>

29. Liu, L., Moriyama, T., Ralph, D. C. & Buhrman, R. A. Spin-Torque Ferromagnetic Resonance Induced by the Spin Hall Effect. *Phys. Rev. Lett.* **106,** 036601 (2011).

30. Mihai Miron, I. *et al.* Current-driven spin torque induced by the Rashba effect in a ferromagnetic metal layer. *Nat. Mater.* **9,** 230–234 (2010).

31. Liu, L., Lee, O. J., Gudmundsen, T. J., Ralph, D. C. & Buhrman, R. A. Current-Induced Switching of Perpendicularly Magnetized Magnetic Layers Using Spin Torque from the Spin Hall Effect. *Phys. Rev. Lett.* **109,** 096602 (2012).

32. Liu, L. *et al.* Spin-Torque Switching with the Giant Spin Hall Effect of Tantalum. *Science* **336,** 555–558 (2012).

33. Pai, C.-F. *et al.* Spin transfer torque devices utilizing the giant spin Hall effect of tungsten.

Appl. Phys. Lett. **101,** 122404–122404–4 (2012).

34. Bychkov, Y. A. & Rashba, E. I. Properties of a 2D electron gas with lifted spectral degeneracy. *JETP Lett* **39,** 78 (1984).
35. Sinova, J. *et al.* Universal Intrinsic Spin Hall Effect. *Phys. Rev. Lett.* **92,** 126603 (2004).
36. Krupin, O. *et al.* Rashba effect at the surfaces of rare-earth metals and their monoxides. *New J. Phys.* **11,** 013035 (2009).
37. Edelstein, V. M. Spin polarization of conduction electrons induced by electric current in two-dimensional asymmetric electron systems. *Solid State Commun.* **73,** 233–235 (1990).
38. Ganichev, S. D. *et al.* Spin-galvanic effect. *Nature* **417,** 153–156 (2002).
39. Manchon, A. & Zhang, S. Theory of spin torque due to spin-orbit coupling. *Phys. Rev. B* **79,** (2009).
40. Pi, U. H. *et al.* Tilting of the spin orientation induced by Rashba effect in ferromagnetic metal layer. *Appl. Phys. Lett.* **97,** 162507 (2010).
41. Alexandradinata, A., Fang, C., Gilbert, M. J. & Bernevig, B. A. Spin-Orbit-Free Topological Insulators without Time-Reversal Symmetry. *Phys. Rev. Lett.* **113,** 116403 (2014).
42. Hasan, M. Z. & Kane, C. L. Colloquium: Topological insulators. *Rev. Mod. Phys.* **82,** 3045–3067 (2010).
43. Zhang, S. Topological states of quantum matter. *Physics* **1,** 6 (2008).
44. Pesin, D. & MacDonald, A. H. Spintronics and pseudospintronics in graphene and topological insulators. *Nat. Mater.* **11,** 409–416 (2012).
45. Burkov, A. A. & Hawthorn, D. G. Spin and Charge Transport on the Surface of a Topological Insulator. *1005.1654* (2010). at <http://arxiv.org/abs/1005.1654>
46. Culcer, D., Hwang, E. H., Stanescu, T. D. & Sarma, S. D. Two-dimensional surface charge transport in topological insulators. *1005.4931* (2010). at <http://arxiv.org/abs/1005.4931>
47. Fischer, M. H., Vaezi, A., Manchon, A. & Kim, E.-A. Large Spin Torque in Topological Insulator/Ferromagnetic Metal Bilayers. (2013). at <http://arxiv.org/abs/1305.1328>
48. King, P. D. C. *et al.* Large Tunable Rashba Spin Splitting of a Two-Dimensional Electron Gas in Bi2Se3. *Phys. Rev. Lett.* **107,** 096802 (2011).
49. Benia, H. M., Lin, C., Kern, K. & Ast, C. R. Reactive Chemical Doping of the Bi2Se3 Topological Insulator. *Phys. Rev. Lett.* **107,** 177602 (2011).
50. Miyamoto, K. *et al.* The gigantic Rashba effect of surface states energetically buried in the topological insulator Bi2Te2Se. *New J. Phys.* **16,** 065016 (2014).
51. Allanson, J. T. The permeability of ferromagnetic materials at frequencies between 105 and 1010 c/s. *J. Inst. Electr. Eng. - Part III Radio Commun. Eng.* **92,** 247–255 (1945).
52. Sankey, J. C. *et al.* Spin-Transfer-Driven Ferromagnetic Resonance of Individual

Nanomagnets. *Phys. Rev. Lett.* **96,** 227601 (2006).

53. Kubota, H. *et al.* Quantitative measurement of voltage dependence of spin-transfer torque in MgO-based magnetic tunnel junctions. *Nat. Phys.* **4,** 37–41 (2008).
54. Sankey, J. C. *et al.* Measurement of the spin-transfer-torque vector in magnetic tunnel junctions. *Nat. Phys.* **4,** 67–71 (2008).
55. Yarislov Tserkovnyak, Arne Brataas & Gerrit E. W. Bauer. Enhanced Gilbert Damping in Thin Ferromagnetic Films. *Phys. Rev. Lett.* **88,** 117601 (2002).
56. Tserkovnyak, Y., Brataas, A. & Bauer, G. E. W. Spin pumping and magnetization dynamics in metallic multilayers. *Phys. Rev. B* **66,** 224403 (2002).
57. Bozorth, R. M. Magnetoresistance and Domain Theory of Iron-Nickel Alloys. *Phys. Rev.* **70,** 923–932 (1946).
58. Jack Sankey. Microwave-frequency characterization of spin transfer and individual nanomagnets. (Cornell University, 2007). at <http://ralphgroup.lassp.cornell.edu/theses/jack_sankey_thesis.pdf>
59. Gregory David Fuchs. Spin-Transfer Effects in Nanoscale Magnetic Tunnel Junctions and Spin Valves. (Cornell University, 2007). at <http://buhrman.research.engineering.cornell.edu/theses/GFuchs.pdf>
60. Mosendz, O. *et al.* Quantifying Spin Hall Angles from Spin Pumping: Experiments and Theory. *Phys. Rev. Lett.* **104,** 046601 (2010).
61. Urban, R., Woltersdorf, G. & Heinrich, B. Gilbert Damping in Single and Multilayer Ultrathin Films: Role of Interfaces in Nonlocal Spin Dynamics. *Phys. Rev. Lett.* **87,** 217204 (2001).
62. Wang, H., Du, C., Hammel, P. C. & Yang, F. Spin current and inverse spin Hall effect in ferromagnetic metals probed by Y3Fe5O12-based spin pumping. *Appl. Phys. Lett.* **104,** 202405 (2014).
63. Nibarger, J. P., Lopusnik, R., Celinski, Z. & Silva, T. J. Variation of magnetization and the Landé g factor with thickness in Ni–Fe films. *Appl. Phys. Lett.* **83,** 93–95 (2003).
64. Mellnik, A. R. *et al.* Spin-transfer torque generated by a topological insulator. *Nature* **511,** 449–451 (2014).
65. Agilent Technologies. Applying Error Correction to Network Analyzer Measurements. at <cp.literature.agilent.com/litweb/pdf/5965-7709E.pdf>
66. Pozar, D. M. *Microwave Engineering*. (Wiley, 2011).
67. Rashba, E. I. Spin currents in thermodynamic equilibrium: The challenge of discerning transport currents. *Phys. Rev. B* **68,** 241315 (2003).
68. Valla, T., Pan, Z.-H., Gardner, D., Lee, Y. S. & Chu, S. Photoemission Spectroscopy of Magnetic and Nonmagnetic Impurities on the Surface of the Bi_{2}Se_{3} Topological Insulator. *Phys. Rev. Lett.* **108,** (2012).

69. Miron, I. M. *et al.* Perpendicular switching of a single ferromagnetic layer induced by in-plane current injection. *Nature* **476,** 189–193 (2011).

70. Niimi, Y. *et al.* Giant Spin Hall Effect Induced by Skew Scattering from Bismuth Impurities inside Thin Film CuBi Alloys. *Phys. Rev. Lett.* **109,** 156602 (2012).

71. King, P. D. C. *et al.* Large tuneable Rashba spin splitting of a two-dimensional electron gas in Bi2Se3. *1103.3220* (2011). at <http://arxiv.org/abs/1103.3220>

72. Bianchi, M. *et al.* Coexistence of the topological state and a two-dimensional electron gas on the surface of Bi2Se3. *Nat Commun* **1,** 128 (2010).

73. Wray, L. A. *et al.* A topological insulator surface under strong Coulomb, magnetic and disorder perturbations. *Nat. Phys.* **7,** 32–37 (2011).

74. Kerr, J. XLIII. On rotation of the plane of polarization by reflection from the pole of a magnet. *Philos. Mag. Ser. 5* **3,** 321–343 (1877).

75. Faraday, M. Experimental Researches in Electricity. Nineteenth Series. *Philos. Trans. R. Soc. Lond.* **136,** 1–20 (1846).

76. Qiu, Z. Q. & Bader, S. D. Surface magneto-optic Kerr effect (SMOKE). *J. Magn. Magn. Mater.* **200,** 664–678 (1999).

77. Zak, J., Moog, E. R., Liu, C. & Bader, S. D. Universal approach to magneto-optics. *J. Magn. Magn. Mater.* **89,** 107–123 (1990).

78. Wohlfarth, E. P. & Buschow, K. H. J. *Handbook of Magnetic Materials*. **13,** (Gulf Professional Publishing, 2001).

79. Peter M. Oppeneer. Theory of Magneto-optics. (2011). at <http://www.ep4.ruhr-uni-bochum.de/imperia/md/content/sfb/summerschool2007/lecture_oppeneer_schwerte.pdf>

80. Hecht, E. *Optics*. (Addison-Wesley, 2001).

81. Višňovský, Š. Magneto-optical ellipsometry. *Czechoslov. J. Phys. B* **36,** 625–650 (1986).

82. Hamrlová, J., Hamrle, J., Postava, K. & Pištora, J. Quadratic-in-magnetization permittivity and conductivity tensor in cubic crystals. *Phys. Status Solidi B* **250,** 2194–2205 (2013).

83. Hamrle, J. *et al.* Huge quadratic magneto-optical Kerr effect and magnetization reversal in the Co2FeSi Heusler compound. *J. Phys. Appl. Phys.* **40,** 1563 (2007).

84. Grabner, L. Longitudinal Hall Effect. *Phys. Rev.* **117,** 689–697 (1960).

85. Fan, X. *et al.* Quantifying interface and bulk contributions to spin-orbit torque in magnetic bilayers. *Nat. Commun.* **5,** (2014).

86. Tristan DeBorde. Scanning Photocurrent Microscopy Study of Photovoltaic and Thermoelectric Effects in Individual Single-Walled Carbon Nanotubes. (Oregon State University, 2014). at <http://www.physics.oregonstate.edu/~minote/Tristan.pdf>

87. Fan, X. *et al.* Observation of the nonlocal spin-orbital effective field. *Nat. Commun.* **4,** 1799 (2013).